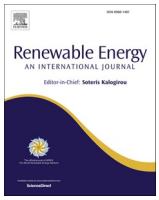
Renewable Energy 219 (2023) 119408



Contents lists available at ScienceDirect

Renewable Energy

journal homepage: www.elsevier.com/locate/renene





A numerical approach to the treatment of submerged water exchange processes through the sluice gates of a tidal power plant

J.W. Kim [a], S.-B. Woo [b,*]

[a] Artificial Intelligence Convergence Research Center, Inha University, Incheon, 22212, Republic of Korea
[b] Department of Ocean Sciences, Inha University, Incheon, 22212, Republic of Korea

ARTICLE INFO

Keywords:
Tidal power generation
Sluice gate
Water exchange
FVCOM
Sihwa tidal power plant

ABSTRACT

Tidal power generation is a sustainable technology for electricity generation and is regulated by water exchange through the hydraulic structures of the tidal power plant (TPP). In the numerical modeling of tidal power generation, the water exchange rate through the sluice gate has previously been estimated based on the water level difference and was input for the entire water column as a two-dimensional boundary condition. However, in this study, a three-dimensional simulation method for the water exchange rate, including submerged hydrological conditions and the momentum of the surrounding flow, was applied. A new numerical approach to water exchange was applied in the idealized tests, and the subsequent model results showed high reproducibility for the orifice velocity field results from laboratory experiments. To verify the hydrodynamics with the actual region, a numerical model was configured for the Sihwa TPP and evaluated through comparison with observation data. The model not only accurately reproduced the temporal variability of the current velocity results, but also reliably reproduced the spatiotemporal flow patterns related to the jet-like and anticlockwise rotating flows. Therefore, to explain the complex, spatiotemporal, and asymmetric flow structure around TPP, high-resolution grid-based 3D modeling technology associated with the submerged sluice gate is needed.

1. Introduction

Tidal power is one of the renewable energy resources and has been in the spotlight as a future energy resource due to its infinite and high predictability. To utilize this energy, tidal power plants (TPPs) have been built in various coastal regions, and as a result, are providing economic benefits for the country through electricity generation [1]. However, as the exchange of seawater between the downstream and upstream regions is artificially blocked by the seawall, it causes significant environmental changes in the surrounding regions [2]. In this study, downstream and upstream refer to the estuary and the reservoir parts, respectively. The potential environmental changes have been predicted through scenario-based studies through numerical modeling in the planning stage before TPP construction [3,4]. For instance, A two-dimensional (2D) finite volume numerical model based on an unstructured triangular mesh was developed to estimate the hydrodynamic effects and flood inundation after the construction of the proposed Cardiff–Weston Barrage, the Fleming Lagoon, and the Shoots Barrage in the Severn estuary [5]. It was concluded that the Fleming Lagoon project would have little impact on the hydrodynamic processes of the Severn Estuary, but other lagoon projects would have significant environmental impacts. Ahmadian et al. [6] also used 1D and 2D models to evaluate the changes in hydrodynamic, sediment transport and water quality processes by the construction of Cardiff–Weston barrage. This study predicts that the operation of the barrage will cause significant changes to the overall environment and ecological conditions of the upstream of barrage. The study suggests that further research should be conducted to assess the potential positive and negative impacts of these changes. Recently, in the case of the La Rance TPP, the 2D depth-averaged numerical model of the Rance estuary was developed to analyze hydrodynamics and tidal wave patterns by the anthropogenically influenced estuarine system [7]. Numerical results indicate that in the absence of TPP, change in bathymetry does not significantly affect the hydrodynamics, while the discharge from the dam significantly modifies the tidal pattern and prisms. These studies are efforts to minimize the negative impacts and maximize the benefits of tidal power generation and are constantly being improved by various researchers.

Most of the studies mentioned above were focused on 2D simulation analysis, and the water exchange rate between the downstream and upstream of the TPP was estimated using the orifice equation derived

* Corresponding author.
E-mail address: sbwoo@inha.ac.kr (S.-B. Woo).

https://doi.org/10.1016/j.renene.2023.119408
Received 11 October 2022; Received in revised form 14 September 2023; Accepted 3 October 2023
Available online 3 October 2023
0960-1481/© 2023 Elsevier Ltd. All rights reserved.

from the Bernoulli energy equation [8,9] as follows:

$$Q = C_d A\sqrt{2gH}, \tag{1}$$

where C_d is the discharge coefficient, A is the cross-sectional area of the sluice gate, g is the gravitational acceleration, and H is the water head difference between the downstream and upstream of the TPP. The estimated water exchange rate was specified for the grids corresponding to the gates, because it was a 2D simulation, the exchange rate change with increasing water depth was not applied. However, in the case of the TPP sluice gate, since it is located underwater, the outflow and inflow of water occur in the lower vertical layer, and as a result, the flow patterns of the upper and lower layers near the sluice gate may be different [10]. Wahl [11] suggested that the calculation error of the water exchange rate derived from the orifice equation could exceed 40% with these underwater flow conditions. In the study of Angeloudis et al. [12], although their work was a 2D simulation analysis, they did not calculate the water exchange rate for the total water depth, but defined the cross-sectional area A according to the height of the sluice gate submerged in the lower layer and calculated the exchange rate of orifice equation accordingly. As a result, the magnitude of the jet-like flow in the 2D simulation results increased, and the formation position changed with an increase in the rotational flow radius. Since the modeling of this study was also 2D, it was not possible to input the difference in the amount of exchange rate by the water depth.

In this study, a 3D numerical approach was attempted to treat the water exchange through the submerged sluice gate of TPP between the upstream and downstream regions together with a high-resolution grid. In addition, a numerical model was constructed by applying this method to the Sihwa TPP. To date, studies of hydrodynamic processes in the Sihwa TPP have been conducted by researchers and various organizations also using numerical models [13,14]. However, these previous model studies used a square grid of 50 m or more around the sluice gate of the Sihwa TPP and exhibited less than 50% reproducibility for the strong flow velocity of 1.5 m s^{-1} or more reported in Kim et al. [15]. Furthermore, their model results have not been verified in terms of the reproduction of flow patterns due to the lack of available spatial and temporal velocity data. Therefore, in order to reproduce the complex flow phenomena near the sluice gate such as vortices, pressure defects near the bed, and jet velocity fields [16–18], cross-sectional information for sluice gates needs to be reflected in the model simulations, and the momentum of the upstream and downstream regions of the TPP in 3D should be calculated in a corresponding high-resolution grid. Some questions regarding the hydrodynamics of the asymmetric flow patterns and anticlockwise rotating flow associated with the operation of the Sihwa TPP remain unanswered.

The purpose of this study is (1) to attempt a new treatment method for the water exchange processes that can incorporate the submerged condition of TPP sluice gates, and (2) to evaluate the performance of this new approach in terms of current speed and velocity field by comparing the results of the idealized test to laboratory experiments, and (3) to verify the capability of the hydrodynamics model using the spatiotemporal field data after applying this method to the Sihwa TPP, and (4) to discuss the impacts of jet-like and rotational flows previously reported in the Sihwa regions.

2. Hydrodynamic model

2.1. Model description

The Finite Volume Coastal Ocean Model (FVCOM) used in this study is a broadly applicable ocean circulation model developed by the University of Massachusetts Dartmouth (UMassD, Dartmouth, MA, USA) and Woods Hole Oceanographic Institution (WHOI, Falmouth, MA, USA) to simulate hydrodynamics and mass transport in the ocean, coastal regions, wetlands, and reservoirs [19]. This model is based on the 3D primitive ocean governing equations, including continuity, momentum, and salt- and heat-balance equations as follows:

$$\frac{\partial u}{\partial t}+u\frac{\partial u}{\partial x}+v\frac{\partial u}{\partial y}+w\frac{\partial u}{\partial z}-fv=-\frac{1}{\rho_0}\frac{\partial P}{\partial x}+\frac{\partial}{\partial z}\left(K_m\frac{\partial u}{\partial z}\right)+F_u, \tag{2a}$$

$$\frac{\partial v}{\partial t}+u\frac{\partial v}{\partial x}+v\frac{\partial v}{\partial y}+w\frac{\partial v}{\partial z}-fu=-\frac{1}{\rho_0}\frac{\partial P}{\partial y}+\frac{\partial}{\partial z}\left(K_m\frac{\partial v}{\partial z}\right)+F_v, \tag{2b}$$

$$\frac{\partial P}{\partial z}=-\rho g, \tag{2c}$$

$$\frac{\partial u}{\partial x}+\frac{\partial v}{\partial y}+\frac{\partial w}{\partial z}=0, \tag{2d}$$

$$\frac{\partial T}{\partial t}+u\frac{\partial T}{\partial x}+v\frac{\partial T}{\partial y}+w\frac{\partial T}{\partial z}=\frac{\partial}{\partial z}\left(K_h\frac{\partial T}{\partial z}\right)+F_T, \tag{2e}$$

$$\frac{\partial S}{\partial t}+u\frac{\partial S}{\partial x}+v\frac{\partial S}{\partial y}+w\frac{\partial S}{\partial z}=\frac{\partial}{\partial z}\left(K_h\frac{\partial S}{\partial z}\right)+F_S, \tag{2f}$$

where x, y, and z are the east, north, and vertical axes of the Cartesian coordinate. u, v, and w are the components in x, y, and z velocity. P is the pressure, ρ is the density, and T and S are the temperature and salinity, respectively. f is the Coriolis parameter and g is the gravitational acceleration. F_u, F_v, F_T, and F_S represent the horizontal momentum, thermal, and salt diffusion terms, respectively. K_m and K_h are the coefficients for the vertical eddy viscosity and diffusion, and they are parameterized using the turbulence sub-model by Mellor and Yamada level-2.5 (MY-2.5) [20]. The Smagorinsky [21] parameterization method is used to estimate the horizontal diffusion coefficients.

FVCOM uses the finite-volume method that discretizes the integral form of governing equations and numerically solves them by flux calculation over an unstructured-grid of triangle. In the FVCOM mesh system, all scalar variables are placed at the nodes of the triangles, whereas velocity components are defined at the center of the triangle. The use of a σ-coordinate in the vertical, where $\sigma=(z-\eta)/D$; η is surface elevation and D is the time-varying total depth, allows for the irregular bathymetry to be mapped onto a model domain. FVCOM uses a mode-splitting method to solve the momentum equations with two distinct time steps of external and internal modes. The external mode consists of a vertically integrated transport equation in which the water level is explicitly solved using a short time step constrained by the ratio of the horizontal resolution and the phase speed of the long gravity wave. The internal mode solves 3D momentum equations and uses a longer time step for the phase speed of the internal wave. These time steps in the external mode and internal mode can efficiently accommodate faster barotropic and slower baroclinic responses. The detailed FVCOM features for the discrete equations and various boundary conditions are described in the FVCOM manual [22].

2.2. Treatment of the water exchange through the sluice gate of the TPP

The FVCOM dike-groyne module in this study was used to simulate the hydrodynamic processes resulting from the operation of the TPP [23]. By treating thin hydraulic structures with kinematic boundary conditions, this module can reproduce a more realistic flow and tracer for the complex currents, water exchange, and turbulent mixing in the area where the submerged structures were installed. To apply this module, a domain decomposition method that decomposes the entire model domain into a downstream domain and an upstream domain relative to the TPP was applied, which has been widely recognized as an efficient method for the simulation of high-resolution physical processes around hydraulic structures [24]. The downstream and upstream domains were hydrodynamically connected through two opposing nodes and cells used in the module (Fig. 1). The solution of the water level (ζ) at the connecting nodes on the wall was calculated during the simulation

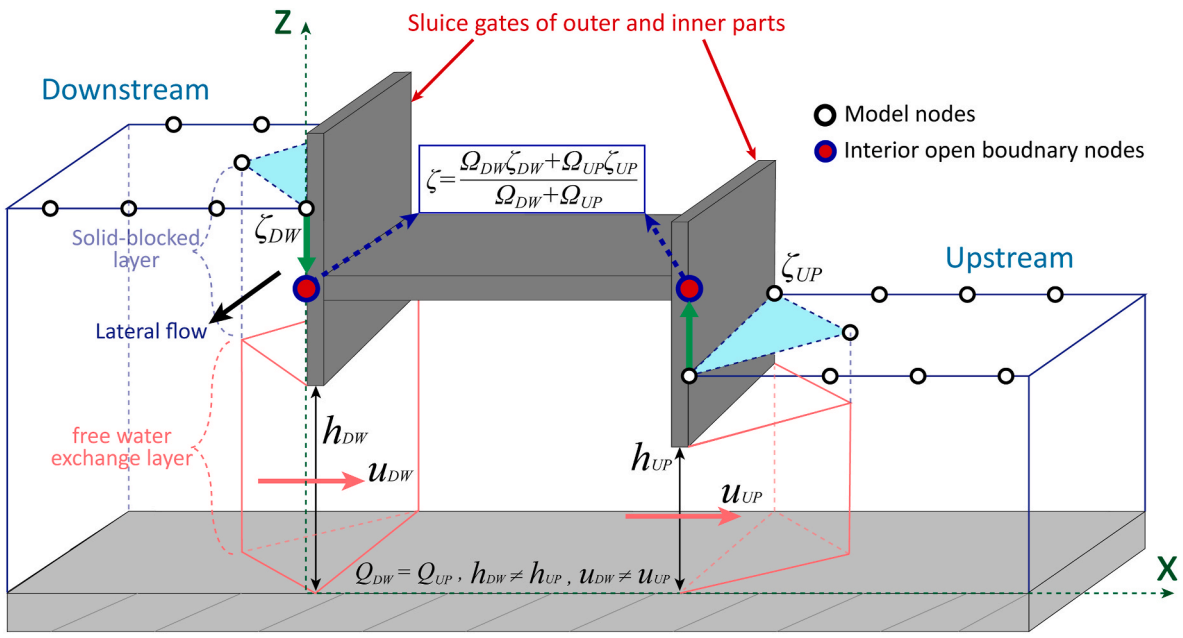


Fig. 1. Schematic representation for explaining the water exchange processes between the downstream and upstream of the sluice gate. The water level and momentum of the two domains were linked by the FVCOM dike-groyne module presented in Ge et al. [21].

as follows:

$$\zeta = \frac{\Omega_{DW}\zeta_{DW} + \Omega_{UP}\zeta_{UP}}{\Omega_{DW} + \Omega_{UP}}, \tag{3}$$

where the subscripts *DW* and *UP* indicate the downstream and upstream sides, respectively. Ω is the area of the connecting cells. The ζ_{DW} and ζ_{UP} are the water level calculated by the water flux at the connecting cells.

The FVCOM dike-groyne module considers the real-time water level and height of gate (h) to determine the submerged vertical layer and using this, the momentum between the upper and lower layers can be calculated. The research of Ge et al. [21] dealt with the process of free momentum exchange within the upper layer, but in this study, the process of free momentum within the lower layer was considered. The horizontal velocity was calculated using the second-order upwind scheme derived by Kobayashi et al. [25], and the boundary conditions of the connecting cells were regarded as a solid wall according to the open or closed state and the height of the sluice gate. For instance, when the hydraulic turbine and sluice gates are closed (e.g., standby phase), the horizontal velocities were treated as a solid wall boundary where the velocity component normal to the solid wall was zero. When the hydraulic turbine and sluice gates are opened (e.g., power generation or drain phases), the velocity was calculated allowing for the free exchange of seawater in the lower layers below the height of the sluice gate ($-\mathrm{H} \leq z < -\mathrm{H} + h$). The velocity towards the wall was treated as zero so that the inflow of seawater in the vertical layer above the height of the sluice gate ($-\mathrm{H} + h \leq z < 0$) was blocked by the solid wall and laterally diverted.

The vertical velocity (ω) in the lower free-exchange layer is calculated as follows:

$$\omega_{i,k+1} = \omega_{i,k} + \frac{\Delta\sigma_k}{\Delta t_I}\left(\zeta_i^{n+1} - \zeta_i^n\right) + \frac{\Delta\sigma_k}{\Omega_{\mathrm{DW}} + \Omega_{UP}} \oint_{l_{DW}+l_{\mathrm{UP}}} u_{N,k}^n D dl, \tag{4}$$

where i, k, and n represent the ith pair of connected nodes, the kth in σ level, and nth time step, respectively. N is an indicator of the velocity component perpendicular to the boundary of a cell with a length of l. Δt_I is the time interval of internal mode. ζ_i^{n+1} is calculated through the vertical integrated continuity equation of external mode. On the other hand, in the upper solid wall layer, ω at the vertical level is calculated separately for the area of DW and UP cells as follows:

$$\omega_{i,k+1}^{\mathrm{DW}} = \omega_{i,k}^{\mathrm{DW}} + \frac{\Delta\sigma_k}{\Delta t_I}\left(\zeta_i^{DW,n+1} - \zeta_i^{\mathrm{DW},n}\right) + \frac{\Delta\sigma_k}{\Omega_{\mathrm{DW}}} \oint_{l_{DW}} u_{N,k}^n D dl, \tag{5a}$$

$$\omega_{i,k+1}^{\mathrm{UP}} = \omega_{i,k}^{UP} + \frac{\Delta\sigma_k}{\Delta t_I}\left(\zeta_i^{UP,n+1} - \zeta_i^{\mathrm{UP},n}\right) + \frac{\Delta\sigma_k}{\Omega_{\mathrm{UP}}} \oint_{l_{\mathrm{UP}}} u_{N,k}^n D dl. \tag{5b}$$

The ω, which is calculated with adjusted internal velocities through these equations, not only guarantees that the volume transport is conservative in the whole water column but also in an individual cell volume in each σ layer.

In numerical modeling, artificial boundaries are introduced to define the extent of the domain when simulating waves or fluid flow in a limited computational region. These boundaries can cause unwanted wave reflections to re-enter the domain, leading to erroneous interference and inaccuracies in the simulation results. A sponge layer is an additional region introduced around the domain boundary [26]. The properties of this region are designed to effectively attenuate the amplitude of outgoing waves when they reach the boundary, by absorbing them. This absorption helps prevent reflections from returning to the domain and reduces the effect of the boundaries on the simulated wave or fluid motion. To consider the energy attenuation near the sluice gate, the sponge layer technique introduced by Kirchner et al. [27] was used in the interior open boundary as follow:

$$u_i^S = \frac{u_i}{1 + c(d)(u_i^2)}, \tag{6a}$$

$$c(d) = c_0 \max\left(1 - \frac{d}{r_S}, 0\right), \tag{6b}$$

where u_i denotes the eastward or the northward velocity component, c is the sponge-layer coefficient in dependency of the distance d toward the nearest boundary grid point and u_i^S denotes the velocity value being further used in the grid element. A sponge-layer coefficient c_0 and a sponge radius r_s are defined for each open-boundary grid point. With rising distance d between the grid element and the open-boundary grid point, for all grid elements in the model domain the sponge-layer coefficient decreases linearly according to the equation. In this study, the meshes connecting the upstream and downstream were fabricated based

on the width of the sluice gate of the Sihwa TPP, 19.3 m. In order to minimize the effect of the velocity attenuation, the sponge layer length related to the treatment of TPP was set to 20 m, which represents the width of the sluice gate.

With this method, the variables related to the hydrodynamics model, such as the surface elevation and current velocity, were directly attenuated at every time step. This sponge layer does not affect the interior solution, only the numerical solution near the boundary. Overall, in this study, the estimated value of the orifice equation for the water exchange rate was not entered as a boundary condition, but the momentum exchange was automatically calculated under internal open boundary conditions by solving the governing equation directly according to the height of the sluice gate in the model. The simulations of the water exchange through the sluice gate of the TPP require large computational resources due to the high-resolution grid (<19.3 m) corresponding to the width of the sluice gate and the short calculation time interval (<0.1 s) for reproducing the strong flow. The FVCOM code decomposes the domain using the METIS graph partitioning libraries, and interprocessor communication uses Message Passing Interface (MPI) calls. In addition, the computational resources for modeling in this study use 28 CPU-cores in each of the 4 nodes.

3. Idealized tests

3.1. Assessing the orifice flow velocity of FVCOM module

To evaluate the capability of the FVCOM dike-groyne module on orifice flow velocity, an idealized rectangular channel was configured for the laboratory experiments presented in Oh et al. [28]. The numerical simulation was performed with almost identical settings to the "Case A″ experiment from their study (hereafter referred to as the Oh-A) (Table 1). The lengths of the channel in the x and y dimensions were 23.6 m and 16.0 m, respectively (Fig. 2a). The model grid consisted of an unstructured triangular mesh, and the horizontal resolution varied from 0.27 m near the sluice gate to about 0.5 m in the open boundary. A total of 81 sigma levels were assigned vertically in the entire grid. As shown in Fig. 2b, the water depth at a distance of 0–0.71 m away from the sluice gate located in the center was 0.32 m, and at a distance of 0.71–2.65 m, the water depth decreased to 0.129 m with a linear slope. The water depth from a distance of 2.65 m to both open boundaries was also 0.129 m with the flat-bottom condition.

The entire model domain was composed of two parts based on the domain center: the left region with the boundary condition of inflow and the right region with the boundary condition of outflow. Both the inflow and outflow rates at the open boundaries were set to a constant of 0.217 $m^3\ s^{-1}$. These two domains were dynamically linked by 20 connecting cells located at the center of the model domain by the FVCOM dike-groyne module (green box in Fig. 2a). The height of the sluice gate was set to 0.182 m, and the gate was open at all times to allow the free exchange of water throughout the entire water column. There is a difference between the width of the gate set up in FVCOM and the width of the gate fabricated in the experiment of Oh-A due to the presence of a thin wall of 0.042 m. When a 0.042 m wall was implemented as a model, the grid resolution became too high, and as a result, the instability increased, and the model results were not realistic. The difference in cross-sectional area caused by a thin wall of 0.042 m is 0.0076 m^2. The horizontal and vertical mixing coefficients of $10^{-5}\ m^2\ s^{-1}$ suggested by Kunze and Sanford [29] were used. Considering the model stability, the total simulation time was set to 3 days with an internal time step of 1 s and an external time step of 0.1 s.

Table 1
FVCOM setup details for the Oh-A.

Properties	Setup values
Number of nodes	2476
Number of cells	4660
Number of connected cell pairs	10
Resolution at open boundaries (m)	0.50
Resolution at connected cell (m)	0.27
Range of water depth (m)	0.13–0.32
Inflow and outflow rates ($m^3\ s^{-1}$)	0.217

The FVCOM results associated with the spatial flow patterns are shown in Fig. 3a. In Fig. 11 of Oh et al. (2016), the current speed in the left domain increased due to the convergence of the flow near the sluice gate. In the right domain, the water passing through the sluice gate formed a fan-shaped flow at the center of the channel, resulting in a rapid increase in current speed. These flow patterns are a jet-like flow derived from the reduction of the conveyance cross-sectional area of the sluice gate and is a well-known representative flow phenomenon in the vicinity of hydraulic structures [30]. These flow patterns were distinctly reproduced by the FVCOM dike-groyne module. The flow in the left domain was entrained toward the sluice gate, and the current velocities of the southern and northern parts increased more than those at the inlet of the sluice gate. In addition, a fan-shaped jet-like flow was formed in the center of the right domain channel. Although there are some differences between Flow-3D and FVCOM results in spatial flow patterns, these key dynamics are functionally calculated. For hydrodynamics in the vicinity of the sluice gate, the results of the Flow-3D model with a third-order numerical scheme has a higher accuracy than the FVCOM using the second-order numerical scheme. This difference in accuracy between FVCOM and Flow-3D may affect the difference in velocity distribution.

In terms of the increase in current speed, the module also predicted the current speed of up to 0.45 m s^{-1} measured with electronic equipment of Oh-A well. The time-series results for the current speed at P1 are presented by the solid black line in Fig. 3b. At the beginning of the simulation, the current speed at P1 reached approximately 0.44 m s^{-1} during a stabilization period of 0.23 days. A stable current speed was then maintained for the remainder of the simulation period, with the variability of 0.07 m s^{-1}. The velocities at ten sluice gates were normalized by spatial mean of the velocities are shown in Fig. 3c. Although there are oscillations in the normalized data, the data at both ends are relatively weak, and in the central region they formed a parabola with the variations of 2–5%. Although not perfectly consistent with Oh-A results, the distribution pattern of these normalized velocity data matches Oh-A's results quite well. For example, the highest normalized velocity was calculated in gate 4 of FVCOM, similar to that measured in gate 4 presented in Fig. 5b of Oh-A. The results of $C_d = Q/A\sqrt{2gH}$ estimated by using the velocities and water head difference of model near the gates were also reliable (Fig. 3d). In the Oh-A, between 0.2 and 0.7 in H, Q increases from 0.01 to 0.022 $m^3\ s^{-1}$, and C_d also increases from 1.3 to 1.43. In FVCOM results, between 0.2 and 0.7 in H, Q increases from 0.012 to 0.0216 $m^3\ s^{-1}$, and C_d also increases from 1.31 to 1.405. The good agreement between these numerical models and laboratory experimental results of Oh-A on the spatial flow patterns, velocity distribution, Q and C_d of the sluice gate suggested that the FVCOM's module can reproduce the hydrodynamics in the TPP system based on the orifice.

3.2. Submerged flow in response to the sluice gate height

To examine whether the module can reproduce 3D submerged flow, an idealized model domain with conditions similar to that of the Sihwa TPP was constructed (Fig. 4). The entire domain was divided into the downstream of 50 × 25 km^2 in correspondence with the Sihwa estuary (downstream) and the upstream of 4 × 8 km^2 corresponding with Lake Sihwa (upstream). These two domains were connected by the FVCOM dike-groyne module, and the width of this connecting grid was 19.3 m, which was composed using a high resolution of the Sihwa TPP gate width. The left side of the connection grid contained cells corresponding to 10 turbine gates, and on the right side, there were cells corresponding

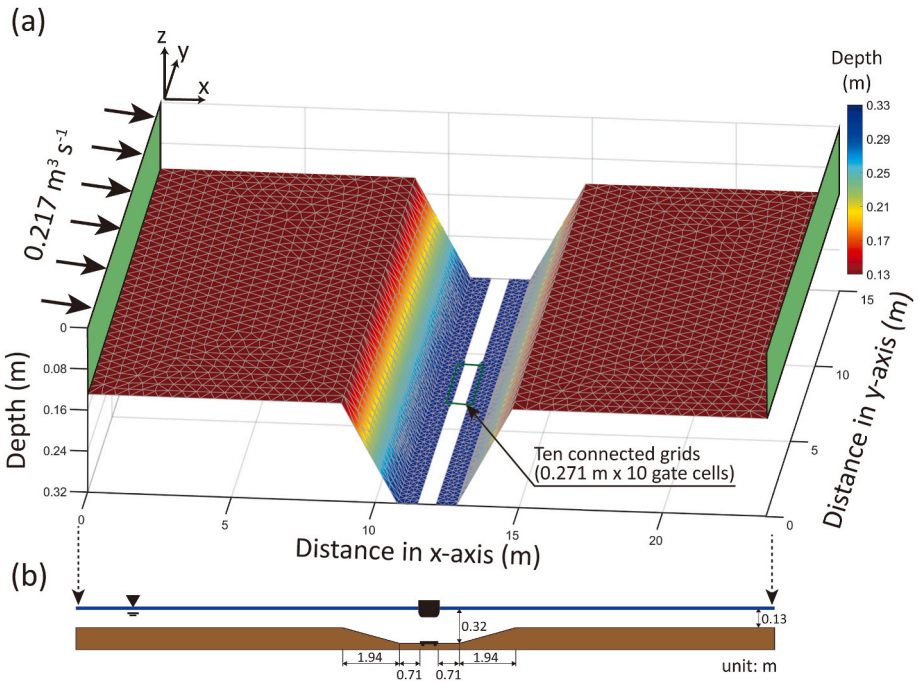


Fig. 2. (a) Idealized model domain configured to test the laboratory experiment of Oh et al. [28], and (b) the side view of the model domain. The left and right light green squares at both ends of the model domain in (a) are the open boundaries for inflow and outflow, respectively. A green box in the center of the domain represents a sponge layer area containing nodes and cells connecting the two domains.

to eight sluice gates without a turbine. In accordance with Bae et al. [31], the heights of the sluice gates without the turbine were set to 12 m both upstream and downstream, whereas those in the downstream and upstream with the turbine were set to 16 m and 14.9 m, respectively.

The seaward open boundary condition was set similarly to that of the Sihwa region. Considering that the tidal propagation in the Sihwa region was from southwest to northeast [32], the location of the seaward open boundary was set to the west. Then, the mean tidal range of 5.5 m in the downstream was input. The water depth was set to 20 m as a flat bottom for the entire area and the sponge ranges and coefficients for all sluice gates were set to 20 m and 0.90, respectively. The total simulation time was 10 days, and the water exchange process was conducted only during the drain phase for 1–3 days to stabilize the model. Additionally, for comparison to evaluate the performance of the submerged flow on the velocity profile, a model case was conducted in which the discharge rate was applied to the entire water column by setting the gate height to 20 m.

The model results for the velocity fields and current speed are shown in Fig. 5. In the tide-predominant regions, spatial vortices can be formed irregularly in addition to jet-like flow, because the discharge direction was oblique compared to the main passage direction of the tidal current [15]. During the drain, a strong jet-like flow was formed in the downstream, and the flow direction turned westward due to the influence of the ebb current from more than 1 km away from the sluice gate. As a result of this horizontally strong velocity shear, the anticlockwise rotating flows with a 1 km radius occurred in the western part of the jet-like flow. The current speed in the upstream during power generation was relatively strong compared to that in the downstream during the drain. However, the current flow mainly propagated in the south, forming a jet-like flow with a greater width compared to during the drain.

The FVCOM dike-groyne module calculates the current velocity differently depending on the height of the submerged sluice gate. The normal velocity profiles in the upstream through the sluice gate between the model results of the case entering the discharge rate into the height of the sluice gate and the model results of the case entering the discharge rate into the entire water column during the drain phase are shown in Fig. 6. In the case of applying the gate height of Sihwa TPP, the normal velocity magnitude for a sluice gate without a turbine (Fig. 6a) was greater than that with a turbine due to a decrease in the cross-sectional area of the gate. Since the gate height was 12 m, the normal velocity magnitude within 8 m depth was also calculated as zero, whereas that reached 1.8 m s^{-1} at 8–20 m depths. At the turbine sluice gate (Fig. 6b), the normal velocity magnitude within 5 m depth was calculated as zero during the drain phase, whereas that reached 1.3 m s^{-1} at 5–20 m depths, corresponding to the gate height. On the other hand, when the discharge rate is applied to the entire water column, The current velocity was calculated in the form of a logarithmic profile affected by typical bottom friction. Since the water volume and momentum is conserved, the depth-averaged velocity is the same in both simulations, but the maximum velocity values in the case where the height of the TPP sluice gate is applied are 10–40% higher. This current velocity increase due to cross-sectional area change is suitable for solving the complex hydrodynamics around the sluice gate. In order to confirm the reproducibility of this process, the FVCOM was applied to the Sihwa TPP case with this module, and model performance was subsequently evaluated through comparative verification with in-situ observation data.

4. Application to the Sihwa TPP

4.1. Regional characteristics of Sihwa TPP

The west coast of South Korea is well-known as a suitable estuary for tidal power generation, and as a result, the Sihwa TPP has been successfully operating there since 2011 [31,33]. The Sihwa TPP is located in the middle of the 11.2 km long Sihwa seawall, with the downstream and upstream of this seawall known as the downstream and upstream (Fig. 7a). The mean water depth here was approximately 13 m. The Liquefied Natural Gas (LNG) reserve base and Incheon New Port are located in the northern part of the TPP, with a sea route for large ships in front of them. The northeastern part is connected to a small river, and the Sorae port and wetlands were formed.

The downstream is a macrotidal environment with an average tidal range of 5.5 m. The tide level exhibited typical semi-diurnal tides with

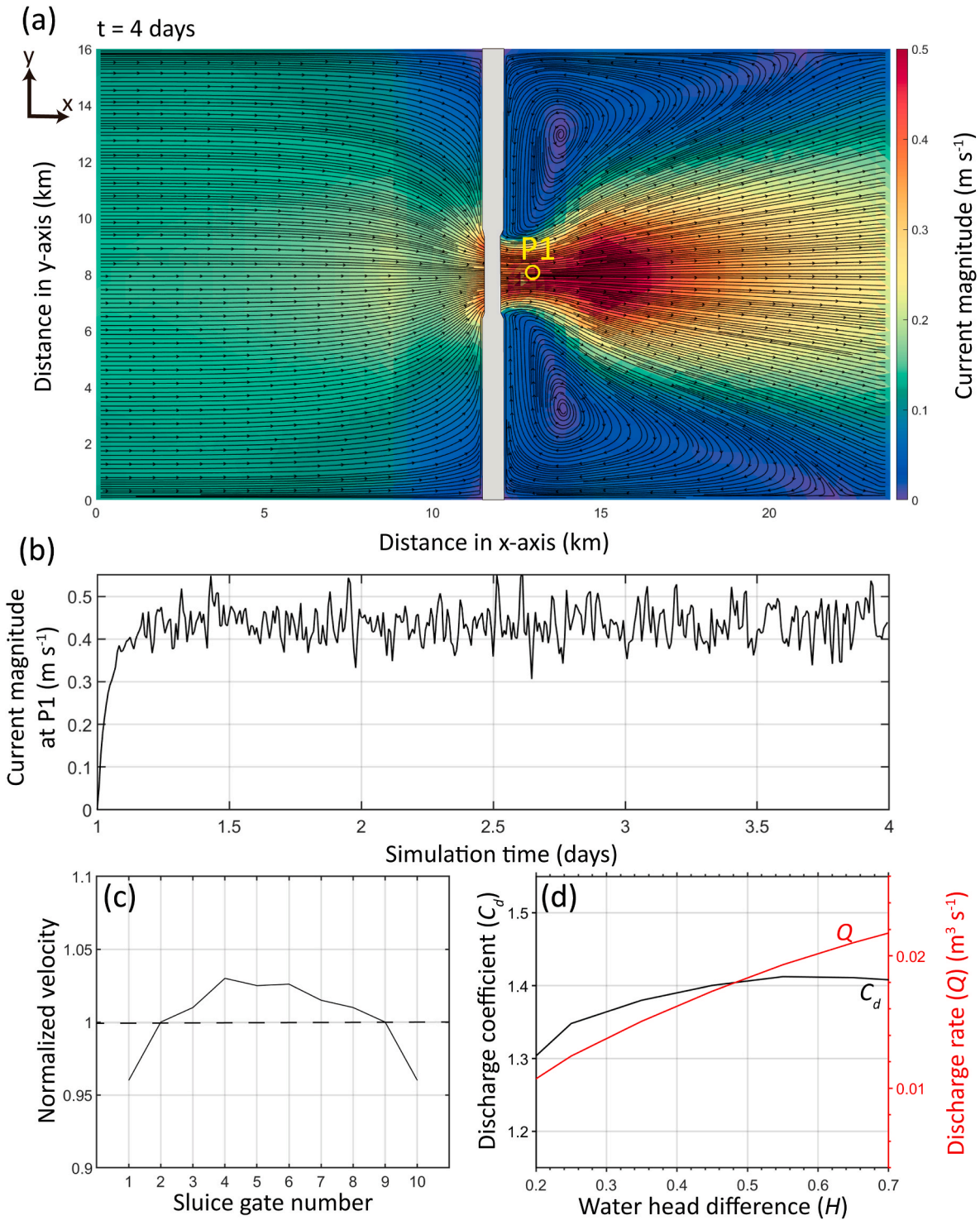


Fig. 3. FVCOM results for Oh-A: (a) snapshot of the spatial flow velocity from day 4, (b) current magnitude variations at P1, (c) normalized velocity at ten sluice gates, and (d) discharge coefficient and rate as a function of the water head difference.

spring-neap variations, and the mean spring and neap tidal ranges were 7.7 m and 3.3 m, respectively. Although the tidal current was artificially suppressed by the seawall, the water level in the upstream showed similar variability to the water level in the downstream through periodic seawater inflow and outflow during tidal power generation. As reported by Kim et al. [34], the amplitude of the water level in the upstream was up to 2 m, more than twice as low as that in the downstream, although spectral analysis in the upstream showed that the five major tidal constituents of M_2, S_2, K_1, O_1, and N_2 were dominant.

The flood generation method of Sihwa TPP is operated in three phases over a tidal cycle: Power generation, drain, and standby. The 10 sluice gates with hydraulic turbines and eight sluice gates with no turbine were used for the exchange of seawater, with a maximum exchange volume of 150 million tons during the power generation and drain phases (Fig. 7b). During power generation (Fig. 7c), as the water level at the downstream raised due to the flood phase, 10 turbine gates were opened to allow the seawater of downstream into the upstream whilst generating electricity through the turbines. Since the upstream region

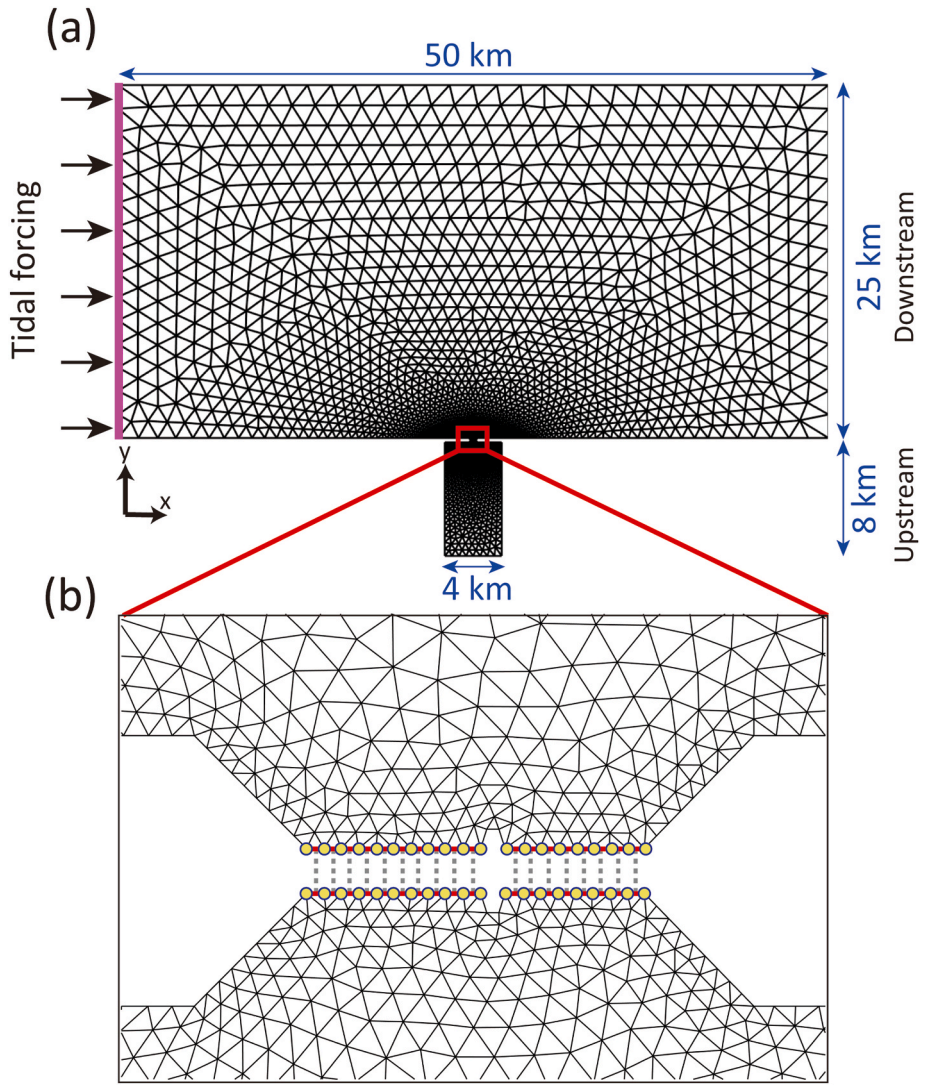


Fig. 4. Idealized model domains to test the reproducibility of the model for the anticlockwise rotating flow. Similarly, to the area of the Sihwa TPP, the entire domain consisted of a scale for two areas: the upstream of Lake Sihwa and the downstream of the Sihwa Estuary.

should not be flooded, power generation is performed up to the maximum water level of −1 m. During the drain phase (Fig. 7d), as the ebb current began and the water level in the downstream was lower than that in the upstream, the seawater in the upstream was discharged into the downstream using the eight sluice gates and 10 turbine gates.

To date, the Sihwa TPP holds the world's largest power generation capacity of 254 MW, contributing significantly to the energy supply with an annual power output of 552.7 GWh [35]. However, the hydrodynamics and sediment dynamics near the Sihwa regions also showed rapid variation due to discharge from Sihwa TPP. After operation of the Sihwa TPP began, the flow velocity and suspended sediment concentration increased by 4.3 and 5.5 times, respectively [15]. As a result, concerns have been raised surrounding the disruption of the safe operation of ships passing through the Incheon New Port and LNG base located in the northern part of the TPP. In addition, the tidal variations in the water level and flow patterns were observed again due to the increase of seawater exchange at upstream [34], and as a result, concerns about flooding in the surrounding private and industrial complexes have increased [36].

4.2. Model setup

The model domain included Gyeonggi Bay and its offshore region as well as the downstream and upstream regions of the Sihwa TPP (Fig. 8a). The coastline of the model domain was constructed using the latest digital charts, topographic maps, and satellite imagery data obtained from the National Geographic Information Institute (NGII). The model grid system had 82096 nodes and 156998 triangular cells in the horizontal direction, with 11 sigma levels in the vertical direction. The depth information of nodes was obtained by the depth data of a digital chart from the Korea Hydrographic and Oceanographic Agency (KHOA), and the depth near the Sihwa TPP was augmented using the bathymetric survey data conducted in 2017. Horizontal resolution varied from 20 m near the Sihwa TPP to approximately 500 m in the bays, before gradually expanding to 4.27 km near the open boundary (Fig. 8b). Based on the Courant-Friedrichs-Lewy (CFL) condition, computational time steps in the external and internal modes were 0.5 s and 2.0 s, respectively. Both initial values of water level and velocity were set to zero. To calculate the friction at the bottom boundary layer, the bottom roughness height (z_0) was set at 0.2 cm.

The seaward open boundary for this study was set up as a water level boundary with the 5 tidal constituents (M_2, S_2, K_1, O_1, N_2) in the region to cover both spring and neap variations. The harmonic constants for the seaward open boundary were extracted from the TPXO09-atlas model results with 1/30 resolution using the tide model driver (TMD) toolbox developed by Oregon State University. The validation results of TMD

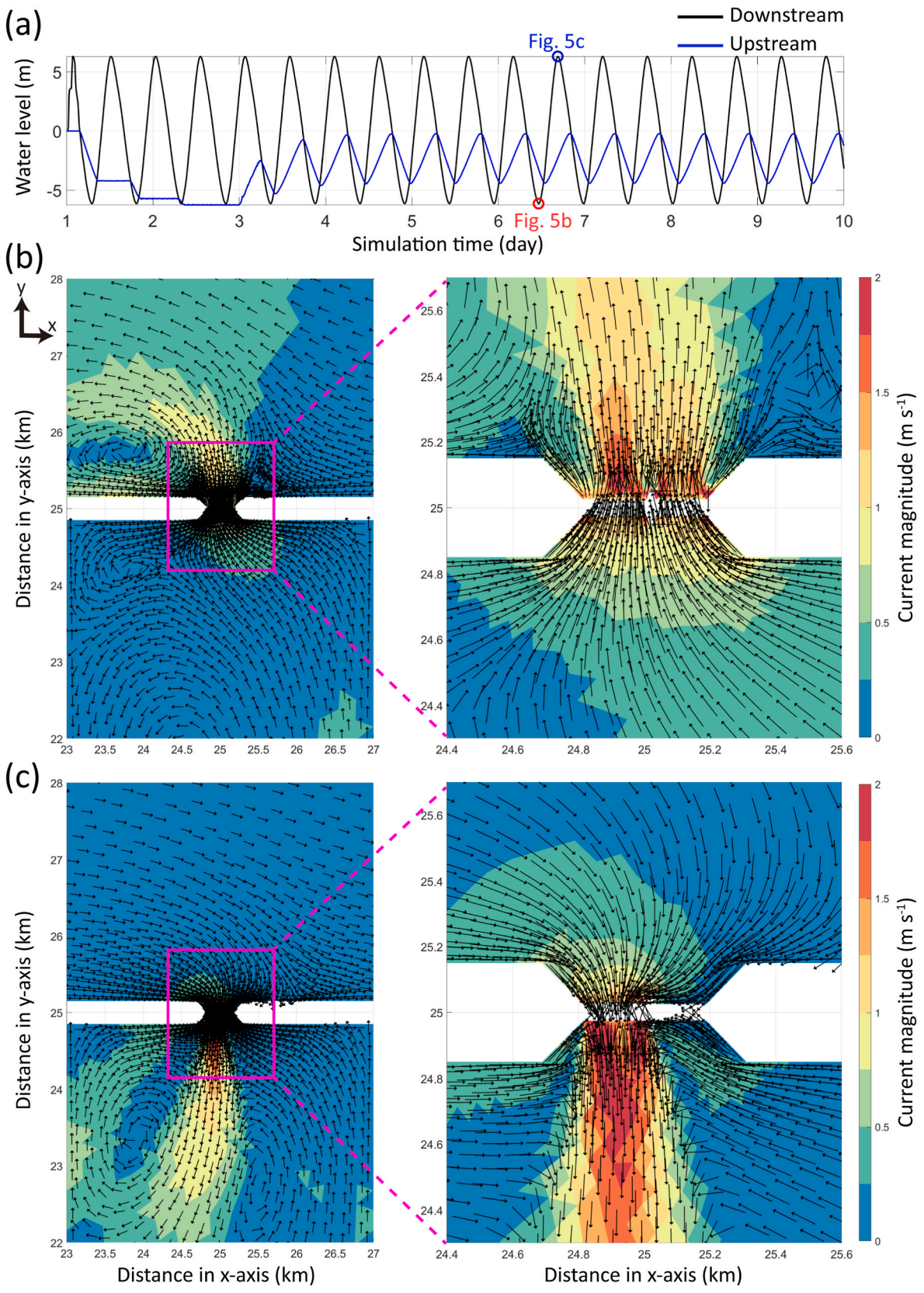


Fig. 5. (a) Model results for the water level of the downstream (black line) and upstream (blue line) adjacent to the sluice gate. The model results for the velocity fields during the (b) drain and (c) power generation phases. Blue and red circles in (a) indicate the period of drain and power generation phases.

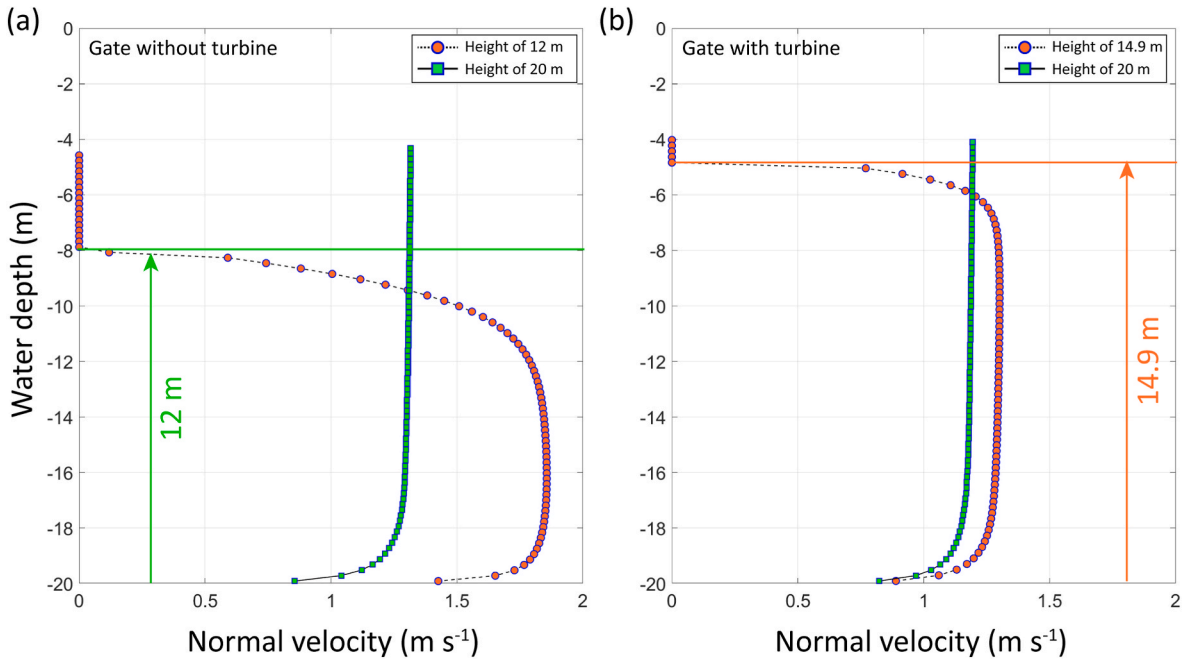


Fig. 6. Comparisons of normal velocity profiles between entering the discharge rate into the height of the sluice gate and entering the discharge rate into the entire water column during drain phase: velocity profiles (a) without and (b) with turbine. the normal velocity refers to the north-south direction component of the velocity.

were presented by Zu et al. [37]. The long- and short-term changes in salinity and temperature observed in the Sihwa region were relatively small [38], and the vertical salinity gradients exhibited almost well-mixed structures ($\triangle S < 0.4$) in response to operation of Sihwa TPP [15]. Since this study is focused on reviewing the performance of the tide model and the water exchange process, we neglected the effect on baroclinic forcings induced by the horizontal density gradients. However, since freshwater is also affected during the monsoon season in this sea area [39], additional studies will be conducted in consideration of salt and water temperature in real-time in future plans after the model evaluation paper on seawater exchange.

The two domains of upstream and downstream were dynamically linked by the FVCOM dike-groyne module (Fig. 8c). The width of the connecting cell was configured with a high resolution of 19.3 m, equivalent to the width of the sluice gate for the Sihwa TPP. The left and right sides of the Sihwa TPP consisted of cells corresponding to 10 turbine gates of 193 m and the eight sluice gates of 154.4 m. The input data for the gate opening and closing times associated with the water exchange were based on the actual operating data obtained from the Korea Water Resources Corporation (http://tlight.kwater.or.kr). The sponge ranges in the connecting grids of the module were set to 20 m, and coefficients for the sluice gate with and without the turbines were 0.9 and 0.6, respectively.

4.3. Model assessment

The water exchange processes during the power generation and drain phases had a significant influence on current speed and spatial flow patterns in the Sihwa region. During the drain phase (Fig. 9a and b), a jet-like flow towards the northwest was formed in the downstream. Flow direction was diverted westward by the interaction of the ebb current within a range greater than 2 km from the TPP, and an anticlockwise rotating vortex was formed on the left side of the jet-like flow. In addition, the water exchange process increased not only the current speed of the surface layer but also the current speed of the bottom layer at least 1.7 m s^{-1}. During power generation (Fig. 9c and d), a jet flow from the upstream to the southeast was formed, although flow velocity strength was weaker by up to 1.1 m s^{-1} compared to the drain phase. In addition, unlike the vortex type generated by one side during the drain, a dipole vortex was formed on both sides of the jet-like flow during power generation. The jet flow associated with such an increase in flow velocity can induce complex flow patterns such as vortex and reverse flow, thereby resulting in asymmetric mass transport.

To verify these model results, the values of the mean error (ME), mean absolute error (MAE), root mean square error (RMSE), normalized RMSE (NRMSE), and predictive skill (Skill) were used for the quantitative assessment between the model results and observations [40]:

$$\mathrm{ME} = \frac{\sum(X_{\mathrm{model}} - X_{\mathrm{obs}})}{N}, \tag{7a}$$

$$\mathrm{MAE} = \frac{\sum|X_{\mathrm{model}} - X_{\mathrm{obs}}|}{N}, \tag{7b}$$

$$\mathrm{RMSE} = \sqrt{\frac{\sum(X_{\mathrm{model}} - X_{\mathrm{obs}})^2}{N}}, \mathrm{NRMSE} = \frac{\mathrm{RMSE}}{X_{\mathrm{obs,max}} - X_{\mathrm{obs,min}}} 100 \tag{7c}$$

$$\mathrm{Skill} = 1 - \frac{\sum|X_{\mathrm{model}} - X_{\mathrm{obs}}|^2}{\sum(|X_{\mathrm{model}} - [X_{\mathrm{obs}}]| + |X_{\mathrm{obs}} - [X_{\mathrm{obs}}]|)^2}, \tag{7d}$$

where X_{model} and X_{obs} are the variables in the model result and observation, respectively, N is the number of observations, and $[X_{\mathrm{obs}}]$ is the time-averaged variable in the observation. ME means that it is possible to confirm whether the model results represent an under-performance or an over-performance. Since MAE represents the absolute value of the error between the observed and model values, if the MAE is low, it would mean that the model performance is good. The RMSE indicates the average difference between the predicted values of the model and the observation values, and NRMSE is similar to RMSE, but has standardized features to prevent errors due to units and size of numbers. The Skill provides the index of the model-data agreement, with Skill = 0 indicating complete disagreement and Skill = 1 representing perfect agreement.

4.3.1. Water level

The model results for water level were evaluated using hourly water level data at 10 tide stations including Gulupdo (P1), Daesan (P2),

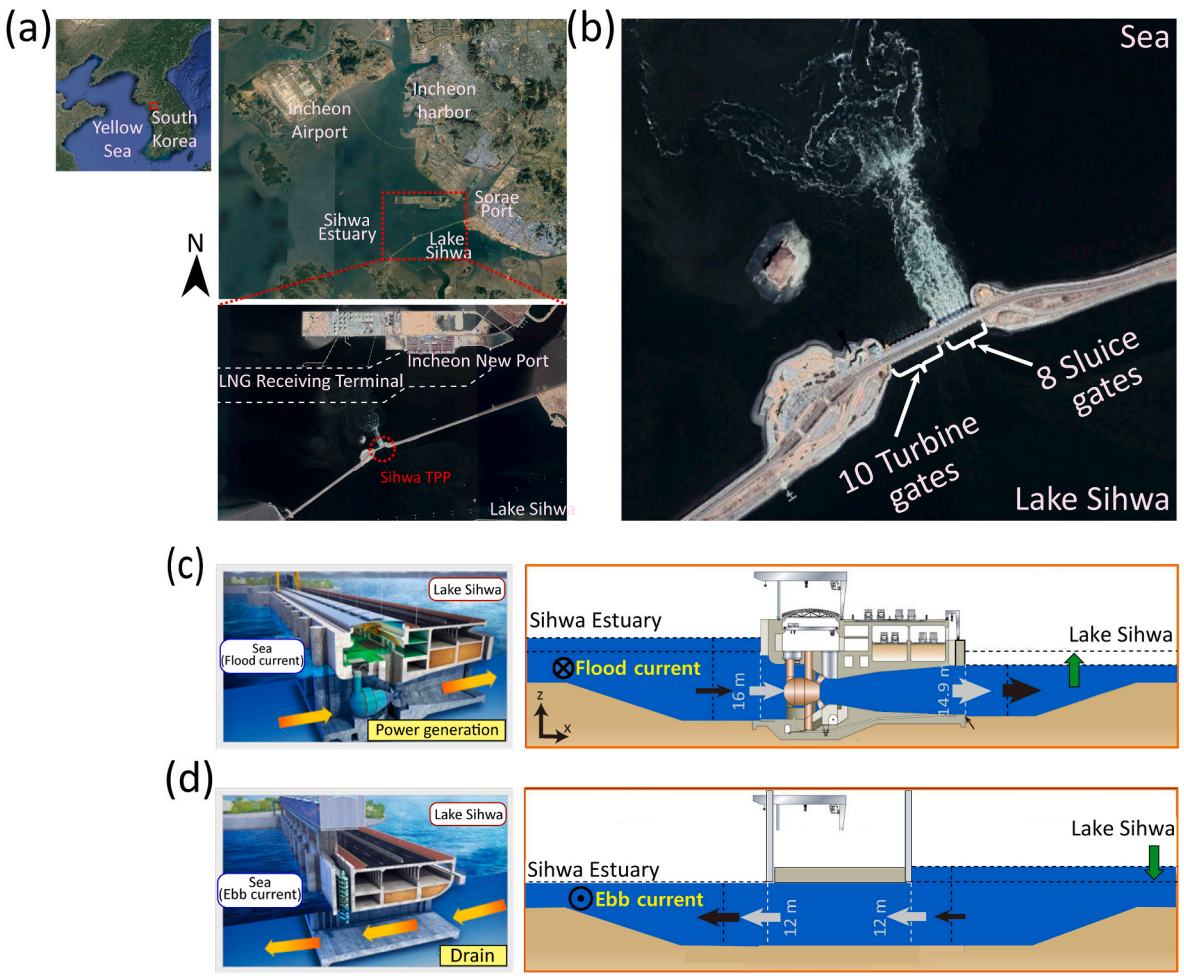


Fig. 7. (a) Location map of the study area, Sihwa tidal power plant (TPP) (red dotted circle), within the frame on the west coast of South Korea, and (b) strong flow during the drain phase captured by satellite (source: Google Earth). The white dotted lines in (a) indicate the sea route for ships passing through LNG Receiving Terminal and Incheon New Port. The gates of TPP consist of 10 turbine gates and the eight sluice gates. Schematics explaining seawater exchange processes during the power generation and drain phases are shown in (c) and (d), respectively (http://tlight.kwater.or.kr).

Pyeongtaek (P3), Yeongheungdo (P4), Ansan (P5), IncheonSongdo (P6), Incheon (P7), Youngjong bridge (P8), Ganghwa bridge (P9), and T-LIGHT station (P10) (red circles in Fig. 8a). The results of the error analysis on the water level are summarized in Table 2. At P1 in the farthest out to sea, the model's water level was underestimated by 2 cm, while the water levels at P2–P9 were overestimated by up to 6 cm. MAE had a low error range of 8–11 cm, and Skill showed a high value of 0.99 for P1–P9. The RMSE at all stations varied between 9 and 14 cm, and NRMSEs of less than 5% were calculated for water level reproduction. In terms of temporal variability, the model also reproduced the water level at P6 close to the Sihwa TPP well, including semidiurnal tide and spring-neap variations (Fig. 10a).

The water level of the model in the upstream also exhibited a rising and falling pattern twice a day from the water exchange process, which agrees with the tide variations observed at P10 (Fig. 11a). Although the water level of the model was underestimated during the spring tide (109–114 days), MA and MAE showed a low error range of −2 to 9 cm, respectively, and Skill was also calculated at a high value of 0.96. As a result, the model reproduced the water level with a good evaluation, so therefore can capture the amplitude and phase of the barotropic tide in the estuary. In addition, since the water exchange rate of the Sihwa TPP was basically determined by the water level difference between the downstream and upstream, the high reproducibility between these models and observations can provide reliable information for momentum calculations.

4.3.2. *Temporal variability of current velocity*

After confirming the model performance on the reproduction of tidal characteristics, the model results were compared with current velocity data of two moorings (M1 and M2) to examine the reproduction of hydrodynamics in response to the water exchange process of the TPP. The data from M1, and M2, at distances of 3 km and 1 km from the TPP, respectively, were collected by Kim et al. [15,34] in November 2014 for the downstream and March 2015 for the upstream. The model run was conducted from November 1, 2014 to August 31, 2015 to cover these observation periods.

The model results for the current velocity variations in the downstream were evaluated to be reliable (Table 3). For the depth-averaged velocities ($\overline{u}$ and $\overline{v}$) at M1 (Fig. 10b–d), ME was small, ranging between −5 to 6 cm s^{-1}, whilst MAE ranged from 11 to 12 cm s^{-1}. The RMSEs for $\overline{u}$ and $\overline{v}$ were 13 and 14 cm s^{-1}, respectively, and the NRMSEs were 15% and 17%, respectively. The model had reasonable Skills of 0.83–0.80 in simulating the $\overline{u}$ and $\overline{v}$, although the model slightly underpredicted $\overline{u}$ while slightly over-predicting $\overline{v}$. Furthermore, the model successfully reproduced periodic velocity peaks of 0.8 m s^{-1} or more associated with the jet-like flow during the ebb current.

Compared to the observation results during the spring tide period of 311 and 315 days, the underestimation of $\overline{u}$ and the overestimation of $\overline{v}$ of the model are related to the reproducibility of the water level in the upstream. In Fig. 11a, although the period is different, it can be seen that the model water level is higher than the observed water level in each

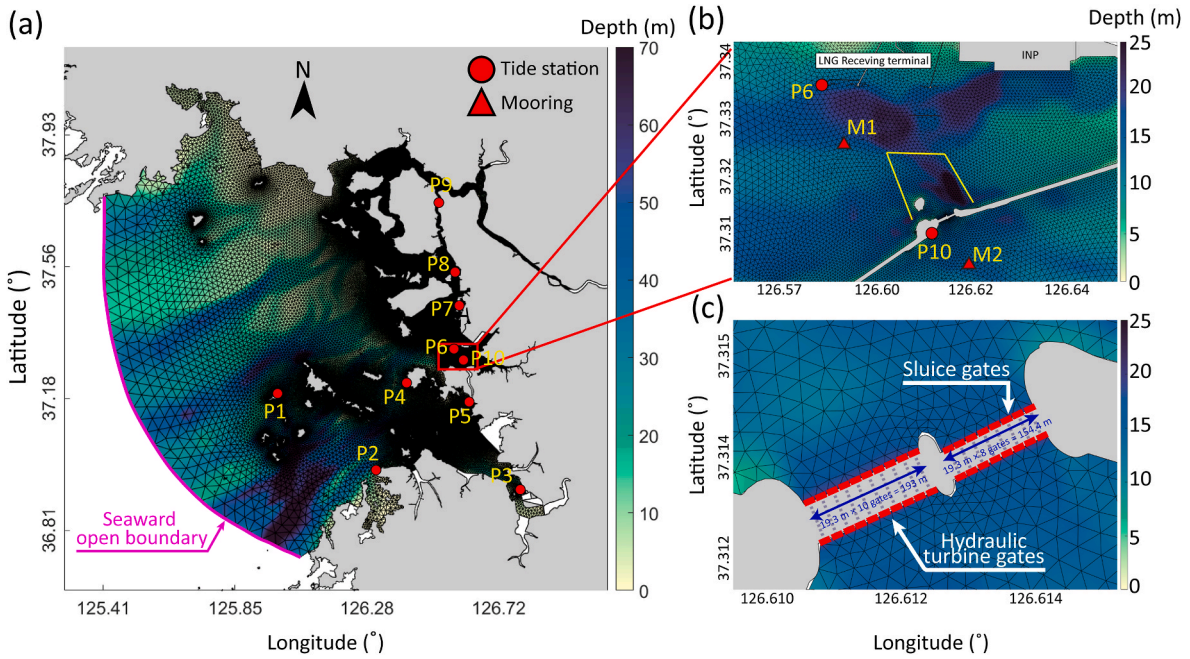


Fig. 8. Model domain with bathymetry and horizontal grid structure. Nine tide stations from the Korea Hydrographic and Oceanographic Agency (KHOA: P1–P9) and one T-LIGHT station in the upstream from the Korea Water Resources Corporation (K-water: P10), and ADCP mooring stations (M1 and M2) and ADCP transect lines (yellow lines) in 2014 and 2015.

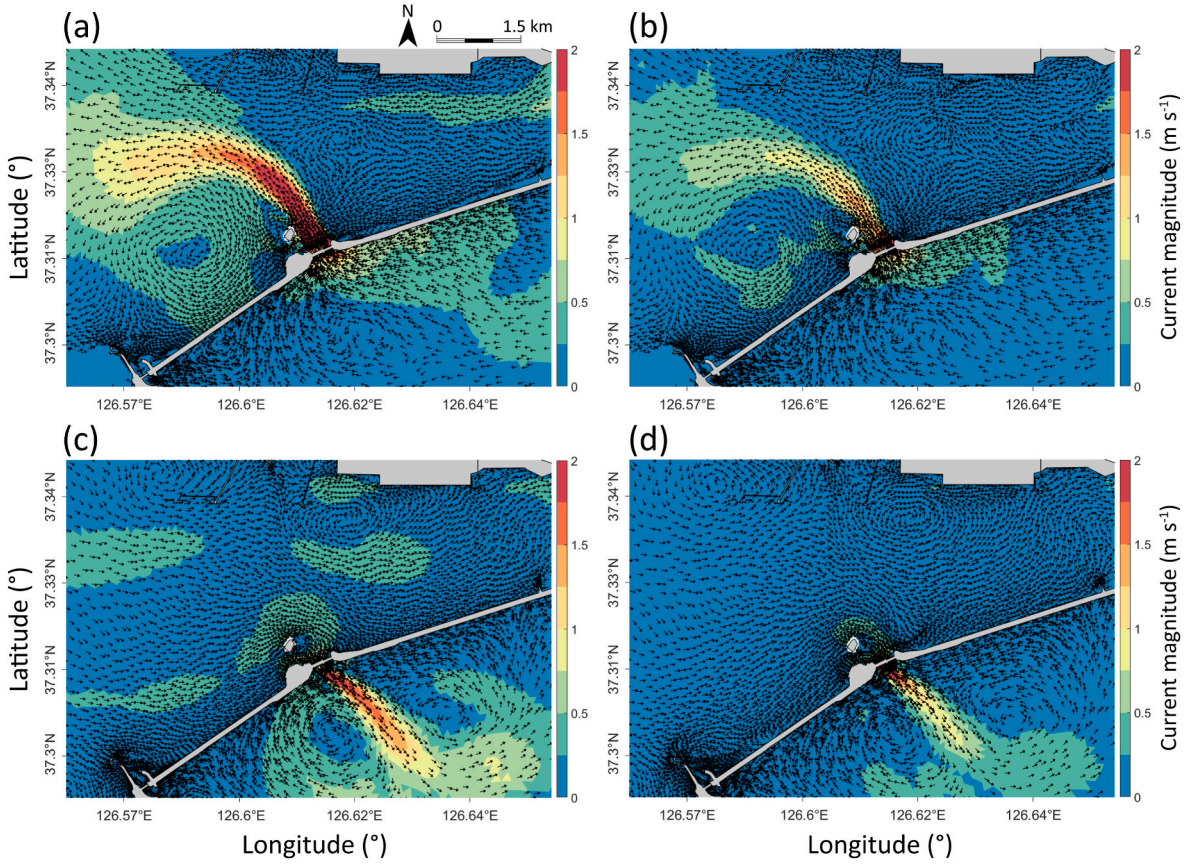


Fig. 9. The model results for near-surface and -bottom velocity fields during (a, b) drain and (c, d) power generation phases. The current speed was shown as a contour, and the magnitudes of the vector plots were normalized.

Table 2
Model assessment for the water levels at P1–P10.

Variable	Station	Location (Latitude/Longitude)	Observation periods	Data resource	ME (cm)	MAE (cm)	RMSE (cm)	NRMSE (%)	Skill
Water level	P1	37°11′40.44″N, 125°59′42.30″E	11/1 in 2014–	KHOA	−2	8	9	1	0.99
	P2	37°0′27.00″N, 126°21′10.00″E	1/25 in 2015		1	8	9	1	0.99
	P3	36°58′0.70″N, 126°49′21.70″E			2	10	12	3	0.99
	P4	37°14′19.00″N, 126°25′43.00″E			1	10	12	3	0.99
	P5	37°11′32.00″N, 126°38′49.93″E			4	12	14	4	0.99
	P6	37°20′17.50″N, 126°35′9.75″E			5	11	13	3	0.99
	P7	37°27′7.14″N, 126°35′31.60″E			2	11	12	3	0.99
	P8	37°32′43.80″N, 126°35′4.10″E			6	11	12	3	0.99
	P9	37°43′55.00″N, 126°31′20.00″E			4	8	10	2	0.99
	P10	37°18′41.89″N, 126°36′38.41″E	4/14–5/6 in 2015	K-water	−2	9	12	3	0.96

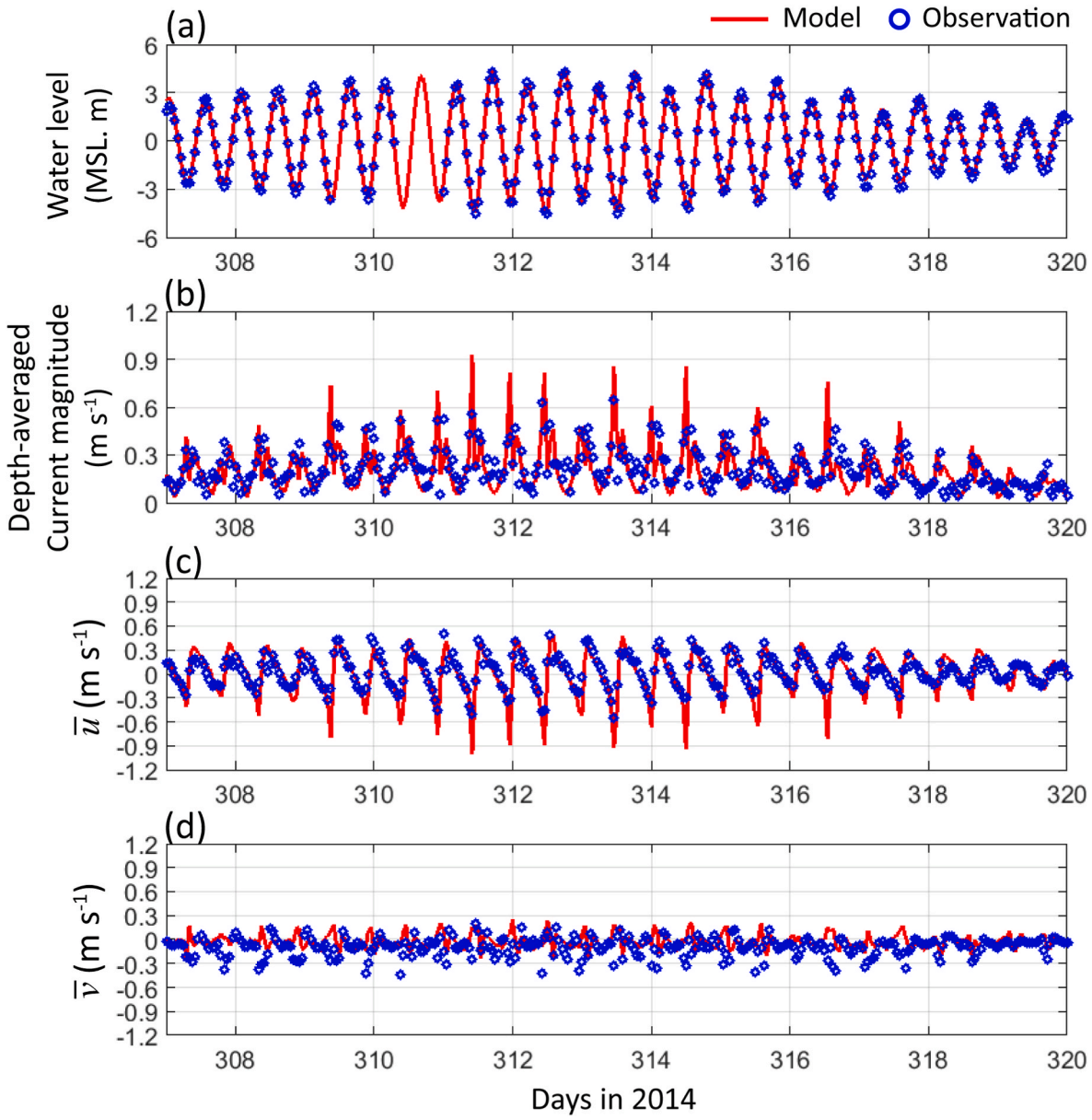


Fig. 10. Comparison of time series results between model and data at M1: (a) water level, (b) depth-averaged current magnitude, (c) east-west and (d) north-south components of depth-averaged velocity. The red lines and blue circles in each panel are model results and observation results, respectively. In (c) and (d), the positive values indicate the depth-averaged velocity towards east and north, respectively.

drain phase for 108–112 days of the spring tide. This means that during the drain phase, the water volume in the upstream was less discharged downstream than actually exchanged water volume. Due to the difference in the range of the jet-like flow that can occur downstream during ebb tide and the resulting rotational flows, the error between the observed flow velocity time series can occur relatively large during the

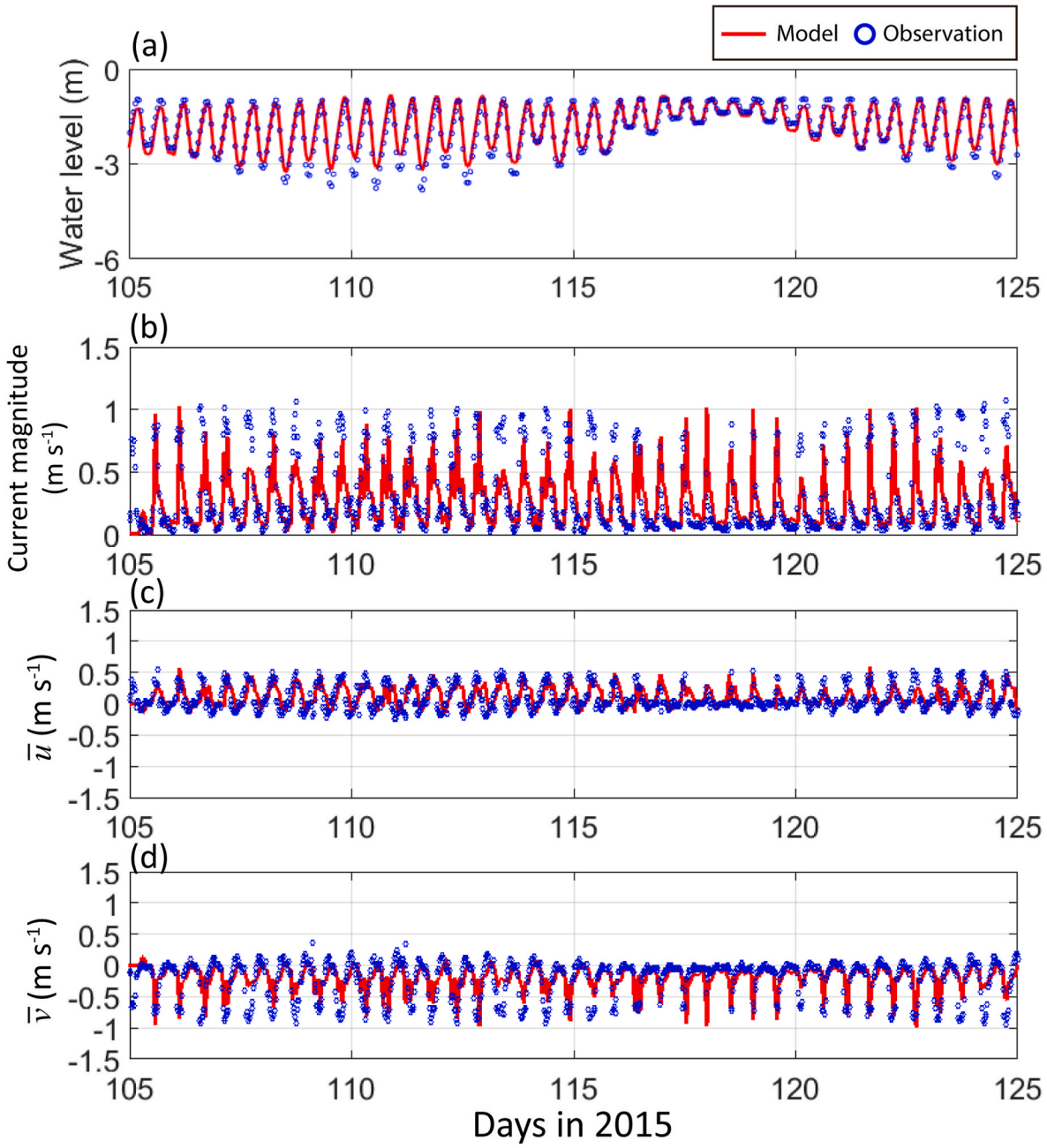


Fig. 11. Comparison of time series results between model and data at M2: (a) water level, (b) depth-averaged current magnitude, (c) east-west and (d) north-south components of depth-averaged velocity. The red lines and blue circles in each panel are model results and observation results, respectively. In (c) and (d), the positive values indicate the depth-averaged velocity towards east and north, respectively.

Table 3
Model assessment for the depth-averaged velocities at M1 and M2.

Variable	Station	Location (Latitude/Longitude)	Observation periods	Data resource		ME (cm s^{-1})	MAE (cm s^{-1})	RMSE (cm s^{-1})	NRMSE (%)	Skill
Current velocities	M1	37°19′37.20″N, 126°35′49.20″E	3/9–4/15 in 2013	ADCP (RDI, 600 kHz)	$\bar{u}$	6	11	13	15	0.83
					$\bar{v}$	−5	12	14	17	0.80
	M2	37°18′17.40″N, 126°37′5.40″E	4/14–5/6 in 2015		$\bar{u}$	−4	7	9	11	0.90
					$\bar{v}$	1	8	10	12	0.87

spring tide. For another reason, since the effect on baroclinic forcings is a modeling result before consideration, it needs to be studied as an improvement in this part in the future.

The model results for the current velocity of the upstream were analyzed to be more accurate than those of the downstream (Fig. 11b–d). In error analysis, for $\bar{u}$ and $\bar{v}$, MA was analyzed as −4 and 1 cm s^{-1}, respectively, while MAE was analyzed as 9 and 5 cm s^{-1}, respectively. The RMSEs for $\bar{u}$ and $\bar{v}$ were 9 and 10 cm s^{-1}, respectively,

and the NRMSE was less than 12%. Skills were 0.90 and 0.87 for each respective velocity component, and high accuracy was derived. Unlike the water level characteristics that showed variability in the spring-neap variations, the temporal variability of the current velocity exhibited the same patterns between spring and neap tides. The peaks of 1 m s^{-1} or more related to the jet-like flow occurred periodically, and this was reproduced by more than 80% in the model. On the other hand, the difference in the velocity peak between the spring and neap tides was 0.1 m s^{-1} or less, and almost the same flow phenomenon occurred. During non-water exchange periods, the current velocity was maintained weakly at less than 0.2 m s^{-1}. Since the upstream flow phenomena were particularly dependent on the water exchange processes, the high reproducibility of current velocity suggested that most temporal variability of the current velocity can be explained more clearly.

4.3.3. Spatial flow patterns and volume transport around the TPP

The model results for flow patterns strongly agreed with observed flow patterns along transects ABCD (Fig. 12) on February 5, 2015. The observation data for flow patterns were obtained by surveys with the ship-mounted acoustic Doppler current profiler (ADCP) presented by Kim et al. [32]. During the drain phase (Fig. 12c–g), the model slightly under-estimated the magnitude of current velocity at transect BC whilst slightly over-estimating the magnitude of current velocity at transect AB. During the power generation phase, the model also reproduced the complex flow structure in transect CD. In particular, for Fig. 12i–k, the model results for reverse flow at the southernmost end of the transect CD were well-matched with the observation results.

The model also accurately reproduced the observed variation in instantaneous normal flux (Q_{inf}) at each transect (Fig. 13). The Q_{inf} of each transect is calculated as follows:

$$Q_{inf} = \iint u_n \bullet dA \tag{8}$$

where u_n is the normal velocity component, and A is the cross-sectional area.

The Q_{inf} at transect AB in the model showed the curve of the tidal wave with a range of -0.9×10^4 to 1.5×10^4 m^3 s^{-1} and had an error range of less than 0.6×10^4 m^3 s^{-1} compared to the observed Q_{inf}. The model Q_{inf} of transect BC, where the effect of the jet-like flow appeared, showed high reproducibility for the observed value of Q_{inf}. The change in Q_{inf} was also well reproduced in the model for the CD transect with the lowest transport volume. Although the observation data include dynamics associated with the tide and water discharge as well as dynamics associated with the wind, temperature, and salinity, the model's capability is sufficient to explore the changes in the temporal and spatial variability of the current velocity in response to the effects of discharge.

5. Discussion

5.1. Complementary points of previous observational studies

In previous observational studies conducted in the downstream, the sediment or mass transport patterns were estimated, but the mechanisms were not identified because the overall spatial flow pattern could not be presented [15,32]. The 3D simulation results satisfying the orifice theory and reflecting an increase in flow velocity with different sluice

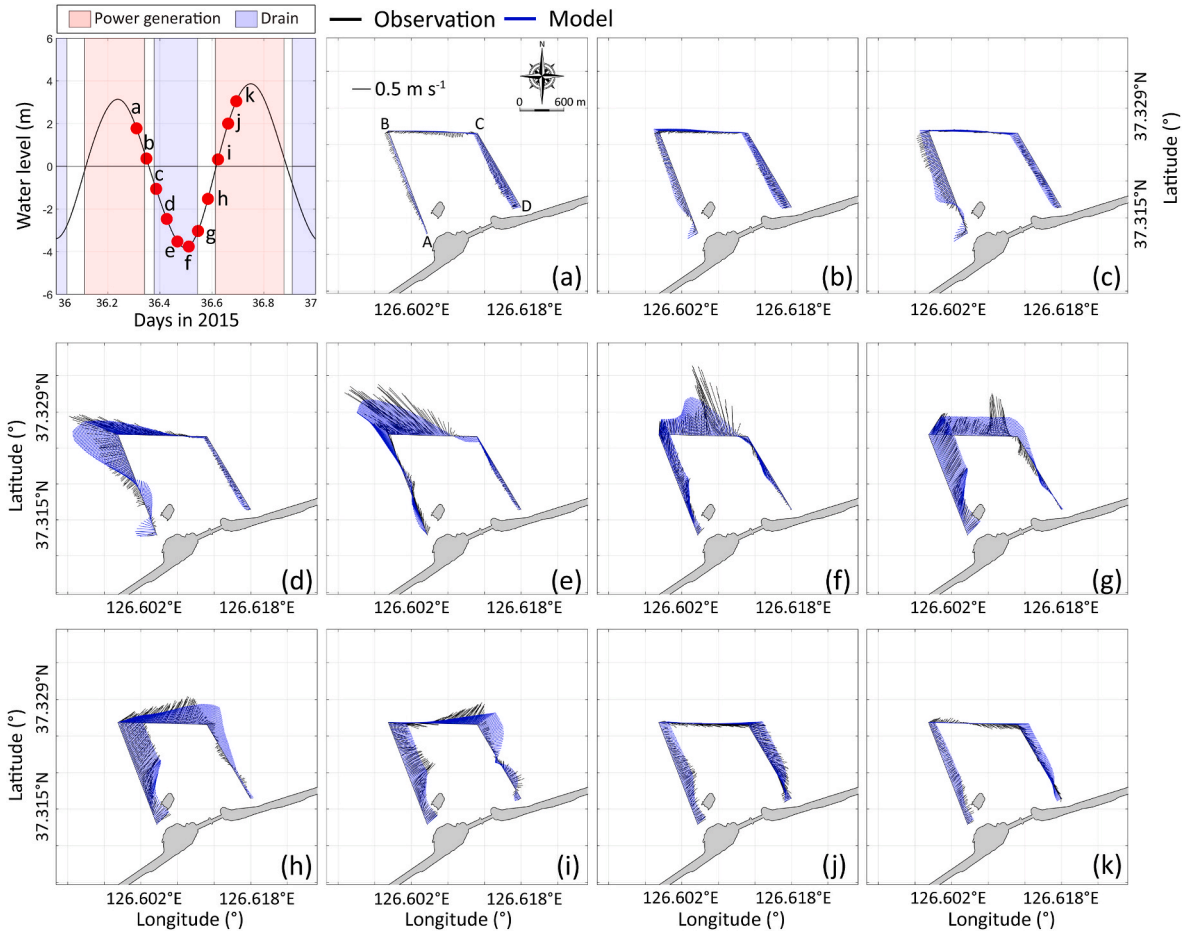


Fig. 12. Model-data comparison for spatial flow patterns over a tidal cycle along ABCD. The observation data were collected on February 5, 2015, and the relevant results were presented in Kim et al. [32]. The black and blue lines indicate the observation results and model results, respectively.

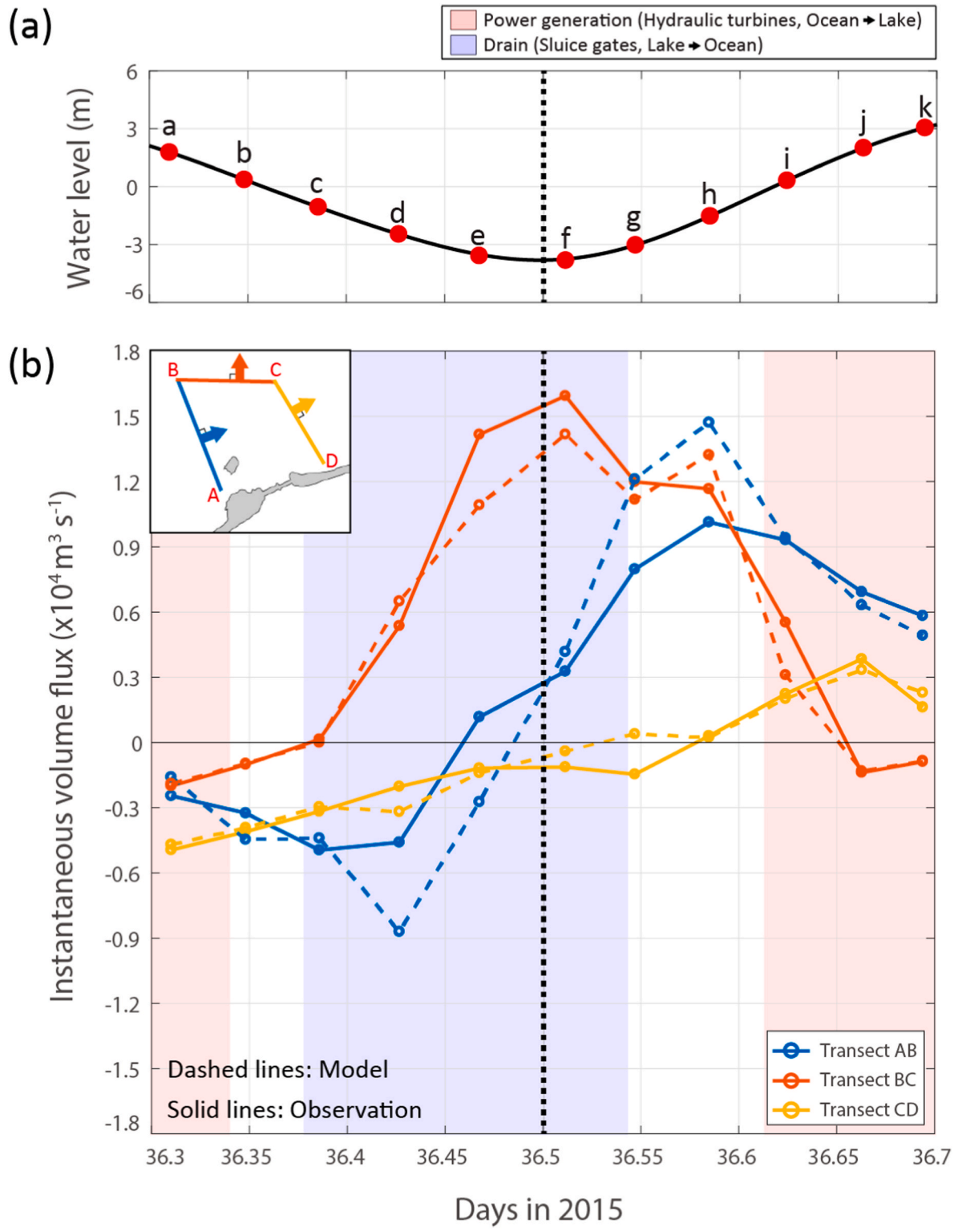


Fig. 13. Model-data comparisons for the instantaneous volume fluxes at transects AB, BC, and CD on February 5, 2015. The black line and red circles in (a) indicate water level variations and observation time, respectively. The dashed and solid lines indicate the model and observation results, respectively. In (b), the arrows in the upper left box represent the direction of the positive normal volume flux of each transect. The black dotted line in (b) represents the low tide.

gate heights can help understand the effects of TPP operation on spatial mass transport of the downstream. First, Kim et al. [15] estimated that the vortex formed by jet-like flow during the drain phase results in only anticlockwise rotating flows, not in the typical dipole form. And when the phase turned to the power generation phase, they estimated that the high concentration of suspended sediment in the drain phase will be directed towards the TPP due to the occurrence of secondary flow. However, in the model results, dipole vortices are formed during the drain phase (Fig. 14a). The vortex in the western region of the jet-like flow has a larger radius and stronger flow intensity than the vortex in the eastern region. During the power generation period, it was evident in the model that as the sluice gates were opened, the surrounding flow was

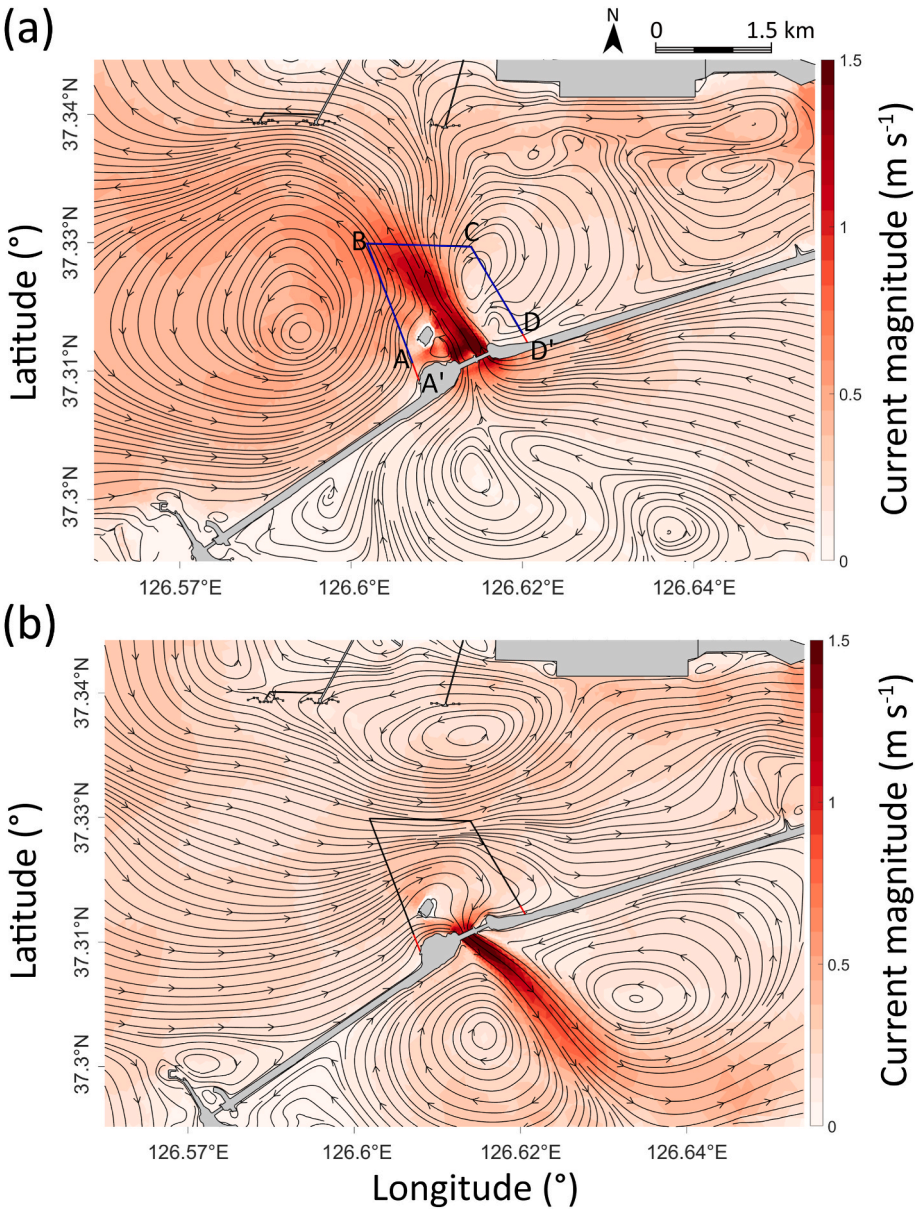


Fig. 14. Mean depth-averaged velocity fields for (a) drain and (b) power generation phases in February 5, 2015. The contour indicates the magnitude of depth-averaged velocity. The streamline indicates the mean flow patterns for drain and power generation.

drawn towards the plant (Fig. 14b). An interesting fact is that not only the flow in the northern part of the island in front of the TPP, but also the flow through the narrow channel in the southern part is strongly drawn towards the turbine gates. This suggests that the main source of concentrated sediments is more likely to be sediments through the southern channel than in the northern channel.

The second unidentified result was that despite the flood current period in which the northeast flow was dominant, the reversed flow towards the southwest occurred at the southern end of the DD' [32]. These flows are related to flow entrainment during the power generation phase. During the power generation phase (Fig. 14b), the current velocity towards the northeast through transect AB is rotated towards the Sihwa TPP in the eastern part of the island. The entrainment flows toward the gate formed inside A'BCD' also affect the flows around the CD, resulting in the reversed flow of DD'. These phenomena are very important issues because of the net substances transport. Since the flows are rotated in CD' equally during the drain period, it means that the flow rotation and reversed flows in CD' derived by the TPP operation inhibit northeastward mass transport during the tidal cycle. In terms of long-term management, the operation of a TPP can be a deterrent to material exchanges in the surrounding waters, resulting in ecological problems.

5.2. *Performance of the model on momentum and volume conservation*

To examine how the momentum and volume exchanged through the sluice gate of the TPP are balanced with those around the downstream, the discharge rate through the sluice gate and the volume fluxes across A'BCD' are shown in Fig. 15. During 46 power generation and drain phase cycles, the water volume was exchanged between the downstream and upstream, and the time-averaged discharge rate was zero. As the duration of the drain phase is shorter than that of the power generation phase, a relatively high discharge rate was calculated. This suggests that treatment techniques of sluice gate conserve momentum and water volume. During the entire period, the time-averaged volume fluxes through A'B and CD' eventually converge into A'BCD' as 2.50 and 0.65 $\times$ 10^3 m^3 s^{-1}, respectively, and these values are completely balanced with -3.15×10^3 m^3 s^{-1} of BC. These balances regarding conservation

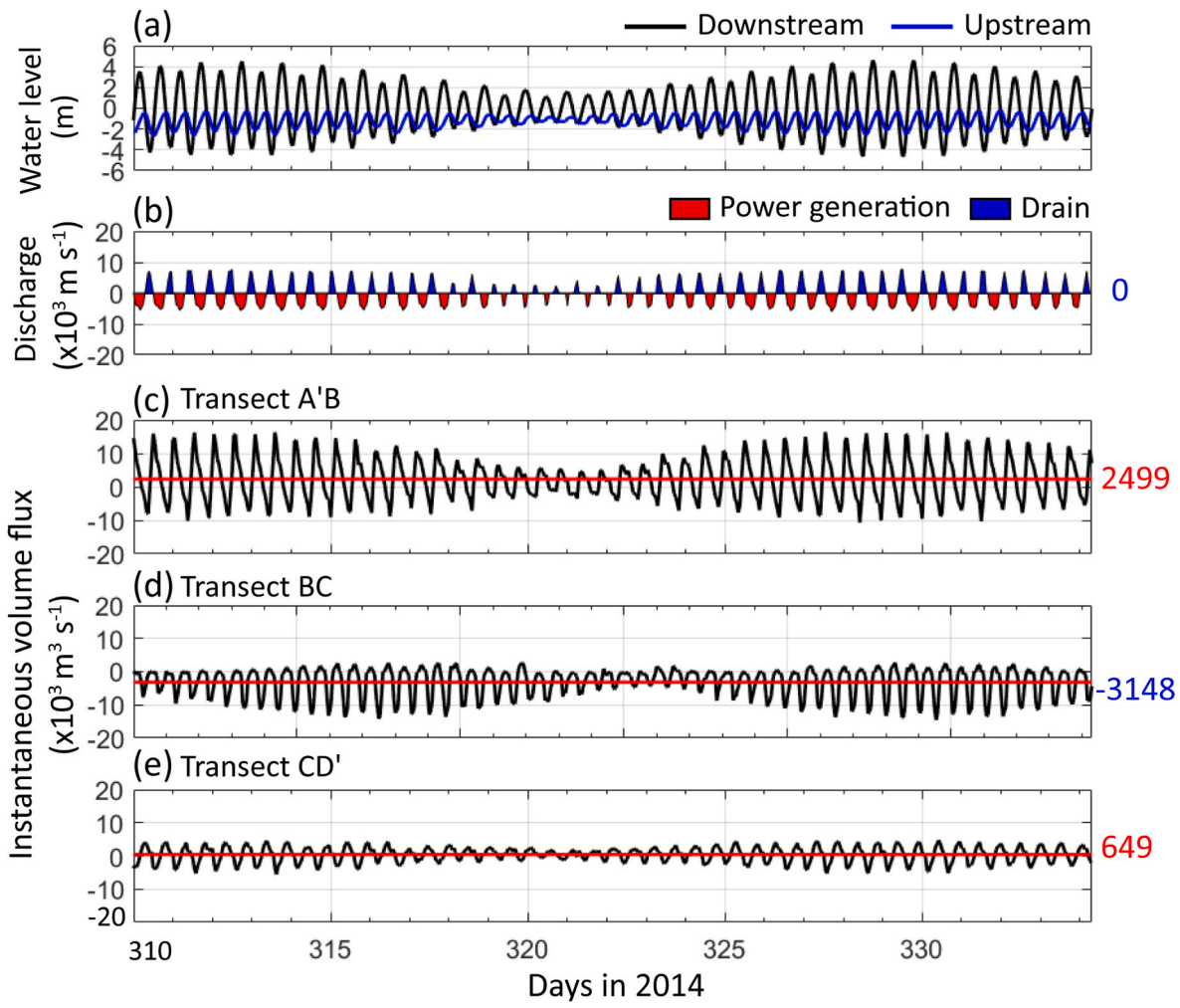


Fig. 15. Comparison of volume fluxes throughout transect A'BCD' to examine the momentum conservation: Time series of (a) water levels of the downstream and upstream, (b) discharge rate of Sihwa TPP between the power generation and drain phases, (c–e) instantaneous volume fluxes (black lines) and time-averaged volume fluxes (red lines) in transects A'B, BC, and CD'. In (b)–(d), the numbers on the right of the figure represent the time-averaged values ($m^3\ s^{-1}$) over the entire period. The positive and negative values of volume fluxes represent the influx and outflux towards the inside of A'BCD', respectively.

between the downstream as well as conservation through the sluice gate imply that the modeling of TPP is functionally performing well.

5.3. Limitations and a future plan

One of the major mechanisms of residual dynamics in estuaries is baroclinic forcing, which is induced by horizontal density gradient [41]. This force develops a two-layer flow structure facing the downstream at the upper layer and upstream at the lower layer. The horizontal density gradient is mainly determined by the inflow of freshwater from land, and the inflow rate varies greatly seasonally [42]. Since our simulation period corresponds to dry season at Sihwa Estuary, there is little effect of fresh water, so water temperature and salt are not considered, but it is essential to consider when performing numerical modeling during the flood season. In addition, the hydrological treatment technology of this study was applied based on the orifice equation, and in the case of turbine operated as an empirical formula through Hill chart, the discharge rate needs to be changed according to the water head difference. Since turbine is currently operated based on Hill chart in Sihwa TPP [34], further research is needed. However, the value of this study is that 3D processing of the sluice gate can increase the current velocity corresponding to the observed current velocity results unlike previous studies, and we will continuously update the related limitations to improve the model.

6. Conclusions

Tidal power prediction technology is an important topic not only in predicting the power output more accurately but also in examining the hydrodynamic impact. In this study, a new methodology was presented for the water exchange rate through the submerged sluice gate of the TPP using the FVCOM of the unstructured grid system. This new treatment technique was used to simulate the hydrodynamic process of the Sihwa regions in response to the water exchange processes of the Sihwa TPP. In addition, the model performance for the hydrodynamics processes was verified through comparison with the time series data measured from 2014 to 2015 adjacent to the TPP. Based on this, the impacts of the tidal power generation on the jet-like flow and material transport were reviewed and discussed. The following conclusions are drawn from this study:

(i) The increase of current velocity due to water exchange at a specific vertical layer of the sluice gate was important for accurate 3D modeling of the hydrodynamic condition related to the operation of the TPP. In this study, the FVCOM dike-groyne model was applied, in which 3D momentum can be fully preserved for both inflow and outflow processes through the submerged sluice gate under the free-surface condition. In the idealized tests, the current velocity of the FVCOM model showed

an error of less than 5% from the current velocity calculated by the orifice equation. On the other hand, as the water exchange was concentrated in the lower layer according to the height of the sluice gate, a stronger flow was calculated in the condition of low gate height than in the high gate height condition.

(ii) Comparing observation data with the model results of the new model for the application of the Sihwa TPP, it can be seen that solving the kinematic boundary condition with a high-resolution grid for the submerged gate was important for reproducing realistic patterns of flow and mass transport in the tidal power generation system. The Sihwa TPP model using the new module associated with the water exchange of the TPP, comprehensively reproduces the temporal variability of observed current velocity.

(iii) The water exchange processes create the jet-like flow structure in the main axis of the channel, all seawater during the drain phase exit through a section of BC. On the other hand, a large-scale rotational mean flow induced a flow along the Sihwa tide embankment, resulting in a flux converging on the jet-like flow. This jet-like flow and the entrainment flow on both sides of the jet suggested that it could be the mechanism for generating the spatiotemporal asymmetric mass transport structure suggested by Kim et al. [15,34].

(iv) In the operation of the plant, the flow pattern around the TPP is dominated by jets and currents due to water exchange, and the nonlinear interaction between the two flows makes the flow characteristics very complicated. Since this behavior is most affected by the water exchange process generated at the sluice gate, it is possible to reproduce the actual flow and material transport pattern only when the momentum and current velocity with a cross-sectional area of the sluice gates are accurately calculated during water exchange. Therefore, to explain the complex, spatiotemporal, and asymmetric flow structure around TPP, it is necessary to concentrate the momentum associated with submerged water flow and consider the characteristics of the related jet-like flow, vortex formation, and mass exchange.

CRediT authorship contribution statement

J.W. Kim: Conceptualization, Methodology, Investigation, Software, Writing – original draft, Writing – review & editing, Visualization. **S.-B. Woo:** Supervision, Conceptualization, Methodology, Project administration, Writing – original draft, Writing – review & editing.

Declaration of competing interest

The authors declare that they have no known competing financial interests or personal relationships that could have appeared to influence the work reported in this paper.

Acknowledgments

This research was supported by Basic Science Research Program through the National Research Foundation of Korea (NRF) funded by the Ministry of Education (NRF-2021R1I1A1A01060397). Also, this research was supported by a National Research Foundation of Korea Grant from the Korean Government (MSIT; the Ministry of Science and ICT) (NRF-2021M1A5A1075516) (KOPRI-PN22013).

References

[1] F. O'Rourke, F. Boyle, A. Reynolds, Tidal energy update 2009, Appl. Energy 87 (2010) 398–409, https://doi.org/10.1016/j.apenergy.2009.08.014.
[2] Y. Wu, C. Xu, Y. Ke, K. Chen, H. Xu, Multi-criteria decision-making on assessment of proposed tidal barrage schemes in terms of environmental impacts, Mar. Pollut. Bull. 125 (2017) 271–281, https://doi.org/10.1016/j.marpolbul.2017.08.030.
[3] B. Guo, R. Ahmadian, R.A. Falconer, Refined hydro-environmental modelling for tidal energy generation: west Somerset Lagoon case study, Renew. Energy 179 (2021) 2104–2123, https://doi.org/10.1016/j.renene.2021.08.034.
[4] A.M. Delgado-Torres, L. García-Rodríguez, Off-grid SeaWater Reverse Osmosis (SWRO) desalination driven by hybrid tidal range/solar PV systems: sensitivity analysis and criteria for preliminary design, Sustain. Energy Technol. Assessments 53 (2022), 102425, https://doi.org/10.1016/j.seta.2022.102425.
[5] J. Xia, R.A. Falconer, B. Lin, Hydrodynamic impact of a tidal barrage in the Severn Estuary, UK, Renew. Energy 35 (2010) 1455–1468, https://doi.org/10.1016/j.renene.2009.12.009.
[6] R. Ahmadian, R. Falconer, B. Lin, Hydro-environmental modelling of proposed Severn barrage, UK, Proc. Inst. Civ. Eng.-Energy 163 (2010) 107–117, https://doi.org/10.1680/ener.2010.163.3.107.
[7] R. Rtimi, A. Sottolichio, P. Tassi, Hydrodynamics of a hyper-tidal estuary influenced by the world's second largest tidal power station (Rance estuary, France), Estuar. Coast Shelf Sci. 250 (2021), 107143, https://doi.org/10.1016/j.ecss.2020.107143.
[8] N. Rajaratnam, K. Subramanya, Flow equation for the sluice gate, J. Irrigat. Drain. Div. 93 (1967) 167–186, https://doi.org/10.1061/JRCEA4.0000503.
[9] C. Baker, P. Leach, Tidal Lagoon Power Generation Scheme in Swansea Bay, Crown, 2006.
[10] E. Kubrak, J. Kubrak, A. Kiczko, M. Kubrak, Flow measurements using a sluice gate; analysis of applicability, Water 12 (3) (2020) 819, https://doi.org/10.3390/w12030819.
[11] T.L. Wahl, Refined energy correction for calibration of submerged radial gates, J. Hydraul. Eng.-ASCE 131 (6) (2005) 457–466, https://doi.org/10.1061/(ASCE)0733-9429(2005)131:6(457).
[12] A. Angeloudis, R.A. Falconer, S. Bray, R. Ahmadian, Representation and operation of tidal energy impoundments in a coastal hydrodynamic model, Renew. Energy 99 (2016) 1103–1115, https://doi.org/10.1016/j.renene.2016.08.004.
[13] Y.S. Kang, Y. Chae, H.R. Lee, Changes in sea water characteristics due to operation of Shihwa tidal power plant, J. Kor. Soc. Coast. Ocean Eng. 25 (4) (2013) 219–235, https://doi.org/10.9765/KSCOE.2013.25.4.219.
[14] Y.H. Bae, B.I. Yoon, C.H. Seo, S.J. Park, K.-Y. Bang, H.-K. Kwon, S.-B. Woo, Residence time variation by operation of Sihwa tidal power plant in outer sea of Sihwa lake, J. Kor. Soc. Coast. Ocean Eng. 29 (5) (2017) 247–259, https://doi.org/10.9765/KSCOE.2017.29.5.247.
[15] J.W. Kim, H.K. Ha, S.-B. Woo, Dynamics of sediment disturbance by periodic artificial discharges from the world's largest tidal power plant, Estuar. Coast Shelf Sci. 190 (2017) 69–79, https://doi.org/10.1016/j.ecss.2017.03.029.
[16] S.-H. Ahn, Y. Xiao, Z. Wang, X. Zhou, Y. Luo, Numerical prediction on the effect of free surface vortex on intake flow characteristics for tidal power station, Renew. Energy 101 (2017) 617–628, https://doi.org/10.1016/j.renene.2016.09.021.
[17] P. Jeffcoate, P. Stansby, D. Apsley, Flow due to multiple jets downstream of a barrage: experiments, 3D computational fluid dynamics, and depth-averaged modeling, J. Hydraul. Eng. 139 (7) (2013) 754–762, https://doi.org/10.1061/(ASCE)HY.1943-7900.0000729.
[18] C.V.M. Vouriot, A. Angeloudis, S.C. Kramer, M.D. Piggott, Fate of large-scale vortices in idealized tidal lagoons, Environ. Fluid Mech. 19 (2019) 329–348, https://doi.org/10.1007/s10652-018-9626-4.
[19] C. Chen, H. Liu, R.C. Beardsley, An unstructured grid, finite-volume, three-dimensional, primitive equations ocean model: application to coastal ocean and estuaries, J. Atmos. Ocean. Technol. 20 (2003) 159–186, https://doi.org/10.1175/1520-0426(2003)020<0159:AUGFVT>2.0.CO;2.
[20] G.L. Mellor, T. Yamada, Development of a turbulence closure model for geophysical fluid problem, Rev. Geophys. 20 (1982) 851–875, https://doi.org/10.1029/RG020i004p00851.
[21] J. Smagorinsky, General circulation experiments with the primitive equations, I. The basic experiment, Mon. Weather Rev. 91 (1963) 99–164, https://doi.org/10.1175/1520-0493(1963)091<0099:GCEWTP>2.3.CO;2.
[22] C. Chen, R.C. Beardsley, G. Cowles, J. Qi, Z. Lai, G. Gao, D. Stuebe, H. Liu, Q. Xu, P. Xue, J. Ge, R. Ji, S. Hu, R. Tian, H. Huang, L. Wu, H. Lin, Y. Sun, L. Zhao, An Unstructured-Grid, Finite-Volume Community Ocean Model FVCOM User Manual, fourth ed., 2013. New Bedford.
[23] J. Ge, C. Chen, J. Qi, P. Ding, R.C. Beardsley, A dike–groyne algorithm in a terrain-following coordinate ocean model (FVCOM): development, validation and application, Ocean Model. 47 (2012) 26–40, https://doi.org/10.1016/j.ocemod.2012.01.006.
[24] J. Xia, R.A. Falconer, B. Lin, Impact of different tidal renewable energy projects on the hydrodynamic processes in the Severn Estuary, Ocean Model. 32 (2010) 86–104, https://doi.org/10.1016/j.ocemod.2009.11.002.
[25] M.H. Kobayashi, J.M.C. Pereira, J.C.F. Pereira, A conservative finite-volume second-order-accurate projection method on hybrid unstructured grids, J. Comput. Phys. 150 (1999) 40–45, https://doi.org/10.1006/jcph.1998.6163.
[26] J. Larsen, H. Dancy, Open boundaries in short wave simulations – a new approach, Coast. Eng. 7 (3) (1983) 285–297, https://doi.org/10.1016/0378-3839(83)90022-4.
[27] J.S. Kirchner, K.A. Lettmann, B. Schnetger, J.-O. Wolf, H.-J. Brumsack, Carbon capture via accelerated weathering of limestone: modeling local impacts on the carbonate chemistry of the southern North Sea, Int. J. Greenh. Gas Control 92 (2020), 102855, https://doi.org/10.1016/j.ijggc.2019.102855.
[28] S.-H. Oh, K.S. Lee, W.-M. Jeong, Three-dimensional experiment and numerical simulation of the discharge performance of sluice passageway for tidal power plant, Renew. Energy 92 (2016) 462–473, https://doi.org/10.1016/j.renene.2016.02.023.

[29] E. Kunze, T.B. Sanford, Abyssal mixing: where it is not, J. Phys. Oceanogr. 26 (1996) 2286–2296, https://doi.org/10.1175/1520-0485(1996)026<2286:AMWIIN>2.0.CO;2.
[30] Y.B. Broekema, R.J. Labeur, W.S.J. Uijttewaal, Observations and analysis of the horizontal structure of a tidal jet at Deep Scour Holes, J. Geophy. Res.-Earth Surf. 123 (2018) 3162–3189, https://doi.org/10.1029/2018JF004754.
[31] Y.H. Bae, K.O. Kim, B.H. Choi, Lake Sihwa tidal power plant project, Ocean Eng. 37 (2010) 454–463, https://doi.org/10.1016/j.oceaneng.2010.01.015.
[32] J.W. Kim, S.-B. Woo, J.I. Song, H.-K. Kwon, An observational study of hydrodynamic impact on water mass transport due to tidal power generation, Sci. Total Environ. 807 (2022), 151013, https://doi.org/10.1016/j.scitotenv.2021.151013.
[33] G. Kim, M.E. Lee, K.S. Lee, J.-S. Park, W.M. Jeong, S.K. Kang, J.-G. Soh, H. Kim, An overview of ocean renewable energy resources in Korea, Renew. Sustain. Energy Rev. 16 (2012) 2278–2288, https://doi.org/10.1016/j.rser.2012.01.040.
[34] J.W. Kim, H.K. Ha, S.-B. Woo, M.-S. Kim, H.-K. Kwon, Unbalanced sediment transport by tidal power generation in Lake Sihwa, Renew. Energy 172 (2021) 1133–1144, https://doi.org/10.1016/j.renene.2021.03.088.
[35] Y.H. Park, Analysis of characteristics of dynamic tidal power on the west coast of Korea, Renew. Sustain. Energy Rev. 68 (2017) 461–474, https://doi.org/10.1016/j.rser.2016.10.008.
[36] M. Kim, B.J. Koo, The intertidal area in Lake Sihwa after operation of the tidal power plant, J. Kor. Soc. Mar. Environ. Energy 18 (2015) 310–316, https://doi.org/10.7846/JKOSMEE.2015.18.4.310.
[37] T. Zu, J. Gan, S.Y. Erofeeva, Numerical study of the tide and tidal dynamics in the south China sea, deep-sea res. Part I-oceanogr, Res. Pap. 55 (2) (2008) 137–154, https://doi.org/10.1016/j.dsr.2007.10.007.
[38] Y. Lee, J. Hur, K. Shin, Characterization and source identification of organic matter in view of land uses and heavy rainfall in the Lake Shihwa, Korea, Mar. Pollut. Bull. 84 (2014) 322–329, https://doi.org/10.1016/j.marpolbul.2014.04.033.
[39] K. Park, J.-H. Oh, H.-S. Kim, H.-H. Im, Case study: mass transport mechanism in kyunggi bay around han river mouth, Korea, J. Hydraul. Eng.-ASCE 128 (3) (2002) 257–267, https://doi.org/10.1061/(ASCE)0733-9429(2002)128:3(257).
[40] C.J. Willmott, On the validation of models, Phys. Geogr. 2 (1981) 184–194, https://doi.org/10.1080/02723646.1981.10642213.
[41] W.R. Geyer, J.H. Trowbridge, M.M. Bowen, The dynamics of a partially mixed estuary, J. Phys. Oceanogr. 30(8) 2035–2048. https://doi.org/10.1175/1520-0485(2000)030<2035:TDOAPM>2.0.CO;2..
[42] H.M. Lee, J.W. Kim, J.Y. Choi, B.I. Yoon, S.-B. Woo, Mechanisms of salt transport in the han river estuary, Gyeonggi bay, J. Kor. Soc. Coast. Ocean Eng. 33 (1) (2021) 13–29, https://doi.org/10.9765/KSCOE.2021.33.1.13.